Doctoral Dissertation

First Principles and Experimental Study of the Valleytronics Properties of Two Dimensional Materials

Kareekunnan Afsal

Supervisor: Prof. Hiroshi Mizuta

Graduate School of Advanced Science and Technology
Japan Advanced Institute of Science and Technology
Materials Science
Sempember 2019

Abstract

It is known for many years that apart from the charge and spin degree of freedom, carriers have yet another degree of freedom known as valley degree of freedom. A per this degree of freedom, the charge carriers residing in the valleys of the band structure of certain materials behave opposite to each other. It also gave rise to a new branch of physics, namely, valleytronics. One of the physical quantity which is used to manipulate and control the valley degree of freedom of the carriers is the Berry curvature. Berry curvature can be understood as a pseudo-magnetic field in the reciprocal space which drives the carriers according to the direction of the Berry curvature resulting in valley current. However, the symmetry arguments of the Berry curvature require either time reversal symmetry or spatial inversion symmetry to be broken for the emergence of Berry curvature. Systems which preserve both these symmetries show no Berry curvature and hence cannot be used as a valleytronic material. Also, an ideal valleytronic material should possess two or more degenerate and in-equivalent valleys in its band structure.

Two-dimensional materials such as graphene and transition metal dichalcogenides, which are of great scientific interest these days have such valleys in their band structure. However, single layer graphene is centrosymmetric. Although AB-stacked bilayer graphene is widely considered to be symmetric, there have been several theoretical studies and experimental observations arguing about an inherent asymmetry persistent in ungated (AB-stacked)bilayer graphene due to electron-electron interaction at low temperatures. However, none of the experimental studies conducted so far have observed Berry curvature induced valley current in ungated (AB-stacked)bilayer graphene, which makes it vital to study the Berry curvature in ungated bilayer graphene. In this study, we observed a non-zero Berry curvature with opposite values at K and K$'$ valleys, validating the argumentation of the asymmetry persistent in ungated (AB-stacked)bilayer graphene. The asymmetry comes from the spontaneous charge transfer to one of the layers as a result of long-range Coulomb interaction between the electrons. This charge imbalance results in a layer asymmetry in the system. Application of an out-of-plane electric field (of the order of μV/nm) reduces the magnitude of the Berry curvature

and dies out at a threshold electric field. When the magnitude of the electric field is increased beyond the threshold value, the Berry curvature reappears but with a change in polarity at K and K′ valleys. This indicates that the polarity of the layer asymmetry also switches beyond the threshold electric field. However, application of higher electric fields (of the order of V/nm) shows a reduction in the magnitude of the Berry curvature with the increase in field strength. As for AA-stacked bilayer graphene, either ungated system or system under out-of-plane electric field did not show any Berry curvature owing to the symmetry present in the system.

Nonetheless, observation of valley current in ungated bilayer graphene is experimentally challenging as it requires ultra clean sample which is isolated from external perturbation. Thus we studied theoretically the possibility of breaking the symmetry in bilayer graphene with the use of hexagonal Boron Nitride (hBN) as a substrate or as an encapsulation layer. Although the role of hBN in breaking the layer symmetry in bilayer graphene and sublattice symmetry in single layer graphene is well known, the effect of the alignment and orientation of hBN layer on the emergence of Berry curvature in these systems is not studied in detail yet. The effect of the out-of-plane electric field is also studied in detail. In the case of bilayer graphene hBN systems the magnitude, as well as the polarity of the Berry curvature, greatly depends on the orientation of hBN layer to the bilayer graphene. This comes from the layer asymmetry induced by the hBN layer in bilayer graphene. Application of an out-of-plane electric field could manipulate the magnitude as well as the polarity of the Berry curvature in these systems. On the other hand, single layer graphene hBN systems are found to be rather insensitive to the configuration of the hBN layer. Although the magnitude of the Berry curvature depends on the alignment of the hBN layer, the orientation of the hBN layer or application of out-of-plane electric field does not impact the polarity of the Berry curvature.

Although the observation of valley current in ungated bilayer graphene which is completely isolated from the external perturbation is difficult, we can utilize the asymmetry induced by the substrate in bilayer graphene to observe valley current. We conducted experimental studies on bilayer graphene exfoliated on Si/SiO_2 substrate in order to detect valley current induced by Berry curvature. The non-local resistance measurement method is employed to detect the valley current. A non-zero non-local resistance was observed in ungated bilayer graphene. The Berry curvature induced valley current is an indication of asymmetry in the system. The asymmetry comes from the potential difference between the layers induced by the substrate. The Ohmic contribution to the non-local resistance was found to be negligible. From the temperature dependent measurements, it was confirmed that the bilayer graphene is gapped and the band gap is calculated to be around 20 meV. The band gap opening substantiates the asymmetry induced by the substrate. On the other hand, measurements conducted on

single-layer graphene did not show any valley current, implying the symmetry persistent in the system.

Keywords: Valleytronics, Berry curvature, Bilayer graphene, hBN, Valley current, Valley Hall effect.

Contents

List of Figures

Chapter 1

Introduction

Electrons have different degrees of freedom. Charge and spin are two of the most known and widely studied degrees of freedom of electrons. As per charge degree of freedom, there can be positive and negative charges and as per the spin degree of freedom, there can be up-spin and down-spin. This freedom to be in either of the two binary states of charge and spin makes them key candidates for the information carrying for memory devices. But the introduction of Berry's phase [1] and related effects have led to the study of yet another degree of freedom in electrons i.e. valley degree of freedom and a brand new branch of research, *Valleytronics* [2, 3]. A local minimum in the conduction band or the local maximum in the valance band is referred to as a *Valley*. An ideal valleytronic material would have more than one valleys in its band structure. This gives the charge carriers the freedom to occupy either of the valleys. Thus valley degree of freedom gives scope for a novel information carrier for memory devices, apart from the charge and spin degree of freedom of the electrons [4, 5]. In recent years, two-dimensional (2D) materials such as graphene and Transition Metal Dichalcogenides (TMDs) have emerged as exemplary candidates for valleytronics study. These materials have two degenerate and in-equivalent valleys at the adjacent corners of the hexagonal Brillouin zone, namely, K and K$'$. Fig. 1.1 shows the band structure of bilayer graphene with K and K$'$ valleys. The electrons in the two valleys can be distinguished by labeling them as valley pseudo-spin up and valley pseudo-spin down.

Berry phase has given rise to various physical properties such as Berry curvature and orbital magnetic moment associated with the Bloch electrons [6]. Both the quantities are present only in those systems where inversion symmetry is broken. Because spatial inversion transforms energetically degenerate K and K$'$ valleys into one another. Berry curvature can be understood as a pseudo magnetic field in the reciprocal lattice which drives the electrons according to the direction of the curvature. A direct

consequence of which is the phenomenon Valley Hall Effect (VHE), where electrons at the two valleys drift to the opposite edges of the materials in the presence of an in-plane electric field due to the equal, but, opposite Berry curvature at the two in-equivalent valleys present in the two adjacent corners of the Brillouin zone [7, 8]. On the other hand, orbital magnetic moment, which originates from the self-rotation of the electron wave packet give rise to a shift in energy in the presence of a perpendicular magnetic field [9, 10].

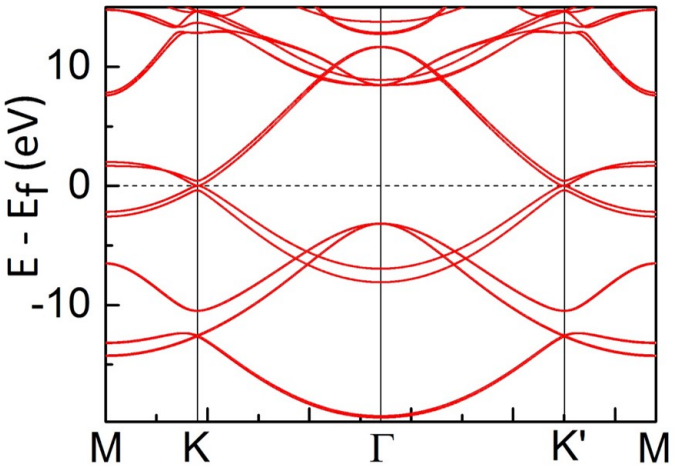

FIGURE 1.1: Band structure of bilayer graphene showing the valleys at K and K′ high symmetry points.

1.1 Berry's Phase

Berry's phase is a *geometric phase* which originates from the *adiabatic change* of the external parameters of a system. This was derived by Professor Michel V. Berry in his seminal paper in 1984 [1]. An almost similar concept was derived for light propagating through a media by Dr. S. Pancharatnam in 1956 [11]. He found that if the polarization state of a light wave changes during its propagation, it acquires an additional phase apart from the dynamical phase. This geometric phase or topological phase is referred to as Pancharatnam's phase of light. In order to understand Berry's phase, we need to be aware of certain concepts such as nonholonomic process, geometric phase, and adiabatic change. Let us have a look at these concepts closely before going into the details of Berry's phase and its implications.

1.1.1 Nonholonomic Process

Examine the motion of the arrow in Fig. 1.2(a). The arrow is moved from the pole to the equator through a longitudinal axis. And then without rotating the

arrow, it is moved along the equator and then moved back to the pole through another longitudinal axis. We can observe that, even though the arrow was not rotated at any point in time, it is no longer pointing in the same direction when it returns to its original position. The arrow is at an angle θ with the initial position of the pendulum. Such a process in which the system does not return to its original position when cycled around a closed loop is called *nonholonomic process* (the motion of the system need not be physical always). This change in direction happens solely due to the geometry of the sphere. It does not depend on the initial direction of the arrow. The same experiment done on a plane surface will end without any change in direction (Fig. 1.2(b)).

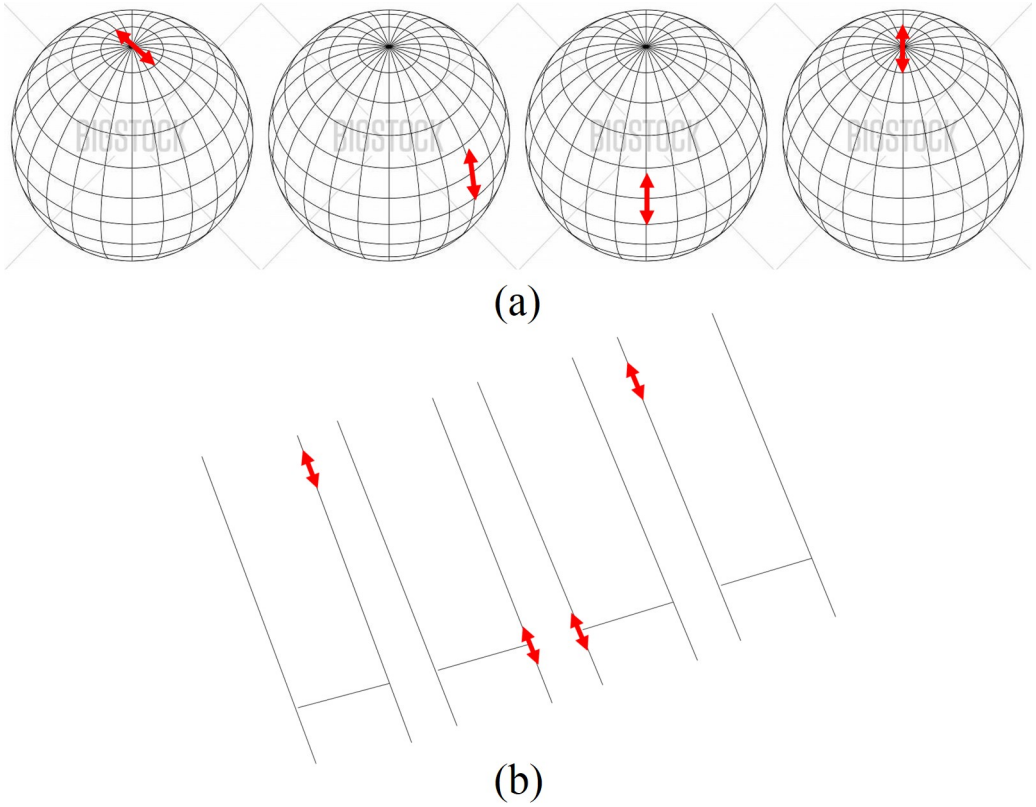

FIGURE 1.2: Motion of an object on the surface of a spherical system results in the change in direction when the object is brought back to the initial position

1.1.2 Adiabatic Theorem

Adiabatic theorem states that a system remains in its ground state if the external parameters governing the system undergoes adiabatic change. The gradual evolution of external parameters acting on a system defines the adiabatic process and the change the system has undergone under adiabatic process is called adiabatic change. Let us consider two situations, one classical mechanical and the other one quantum mechanical, where the system undergoes adiabatic change.

Classical Adiabatic Process

Consider a simple pendulum hanging from the roof inside a train as shown in Fig. 1.3.

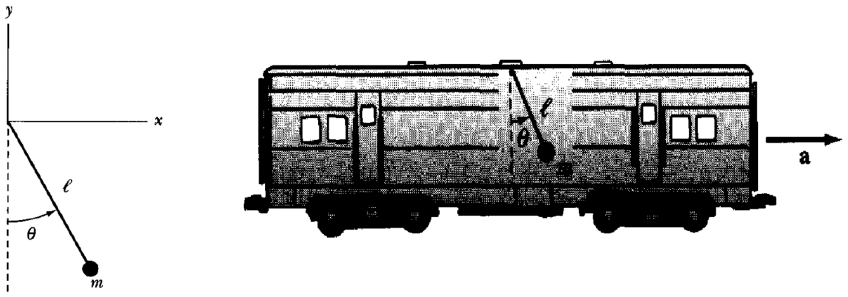

FIGURE 1.3: Schematic diagram showing a pendulum hanging inside a train. Figure taken from Ref. [12]

If the train is stationary, the frequency of oscillation of the pendulum is given by,

$$\omega = \sqrt{\frac{g}{l}}$$

Whereas, if the train is moving with an acceleration a, the frequency of oscillation of the pendulum also varies accordingly and is given by,

$$\omega = \left(\frac{\sqrt{a^2 + g^2}}{l}\right)^{\frac{1}{2}}$$

The pendulum oscillates with a higher frequency as the acceleration of the moving train also adds up to the gravitational acceleration. Now suppose that the train moves very slowly such that the velocity of the train tends to zero ($v \to 0$). In that case the acceleration also tends to zero ($a \to 0$) and the frequency of oscillation of the pendulum changes as,

$$\omega = \left(\frac{\sqrt{a^2 + g^2}}{l}\right)^{\frac{1}{2}} \qquad \xrightarrow{a \to 0} \qquad \omega = \sqrt{\frac{g}{l}}$$

This means that, even though the train is moving from one point to another since the change is very slow (or adiabatic), the frequency of oscillation of the pendulum remains unaltered.

Quantum Adiabatic Process

Consider a molecule which is a collection of constantly moving electrons and nuclei. Since the proton is highly massive than electrons ($\frac{m_p}{m_e} \approx 1836$), the nuclei can be considered

to move much slower than the electrons. Hence it can be said that the electron evolves adiabatically in the environment constituted by the nuclei.

Another interesting example of quantum adiabatic process is extension of box width in particle in a box problem. Imagine a particle in the ground state of an infinite square well with width a. The eigenstate of the particle is (Fig. 1.4(a)),

$$\psi_i(x) = \sqrt{\frac{2}{a}} \sin\left(\frac{\pi}{a}x\right)$$

Now, if we gradually move the right side wall of the well to the position $2a$, according to adiabatic theorem, the particle remains in the ground state of the expanded infinite well. Hence the final state of the paricle is given by(Fig. 1.4(b)),

$$\psi_f(x) = \sqrt{\frac{1}{a}} \sin\left(\frac{\pi}{2a}x\right)$$

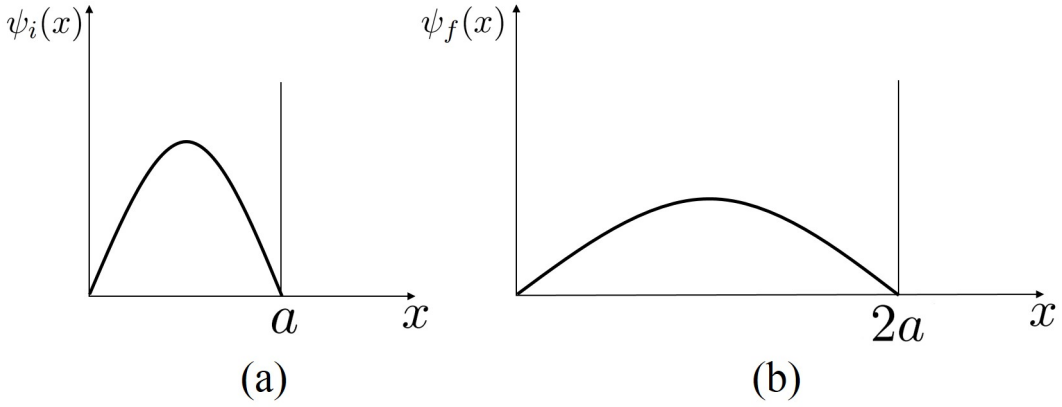

FIGURE 1.4: (a) Wave function corresponding to the ground state of particle in an infinite well of width a. (b) If the right side wall of the particle moves very slowly to the position $2a$, the particle remains in the ground state of the expanded infinite well.

This implies that, since the change in Hamiltonian was slower, the particle remained in the ground state even though the width of the well increased from a to $2a$. Note that this change is not as small as in perturbation theory, but a large change. Also, note that the energy is not conserved here. Whatever is moving the wall is taking energy from the system [13].

1.1.3 Geometric Phase

The adiabatic theorem states that if the Hamiltonian is independent of time, a particle which starts out in the n^{th} state remains in the state after time t apart from

a phase factor,

$$\Psi_n(t) = \psi_n e^{-iE_n t/\hbar} \tag{1.1}$$

If the Hamiltonian is time dependent, then the eigenvalues and eigenfunctions are also time dependent,

$$H(t)\psi_n(t) = E_n(t)\psi_n(t) \tag{1.2}$$

But these eigenfunctions constitute a complete and orthonormal set. Thus, the general solution to the time-dependent Schrödinger equation

$$i\hbar\frac{\partial}{\partial t}\Psi(t) = H(t)\Psi(t) \tag{1.3}$$

can be written as a linear combination of the components of the set,

$$\Psi(t) = \sum_n c_n(t)\psi_n(t)e^{i\theta_n(t)} \tag{1.4}$$

where,

$$\theta_n(t) = -\frac{1}{\hbar}\int_0^t E_n(t')dt' \tag{1.5}$$

is the standard phase factor in the case where E_n varies with time. $\theta_n(t)$ is also known as the *dynamic phase*.

Substituting Eq. 1.4 into Eq. 1.3 gives,

$$i\hbar\sum_n \left[\dot{c_n}\psi_n + c_n\dot{\psi_n} + ic_n\psi_n\dot{\theta_n}\right]e^{i\theta_n} = \sum_n c_n(H\psi_n)e^{i\theta_n} \tag{1.6}$$

The last two terms cancel due to Eq. 1.2 and Eq. 1.5. Thus we have,

$$\sum_n \dot{c_n}\psi_n e^{i\theta_n} = -\sum_n c_n\dot{\psi_n}e^{i\theta_n} \tag{1.7}$$

Taking the inner product with ψ_m,

$$\sum_n \dot{c_n}\delta_{mn}e^{i\theta_n} = -\sum_n c_n\langle\psi_m|\dot{\psi_n}\rangle e^{i\theta_n} \tag{1.8}$$

or

$$\dot{c_m}(t) = -\sum_n c_n\langle\psi_m|\dot{\psi_n}\rangle e^{(i\theta_n-\theta_m)} \tag{1.9}$$

Now to find the inner product $\langle\psi_m|\dot{\psi_n}\rangle$ we differentiate Eq. 1.2 and take the inner product with ψ_m,

$$\langle\psi_m|\dot{H}|\psi_n\rangle + \langle\psi_m|H|\dot{\psi_n}\rangle = \dot{E_n}\delta_{mn} + E_n\langle\psi_m|\dot{\psi_n}\rangle \tag{1.10}$$

We can write $\langle\psi_m|H|\dot{\psi_n}\rangle = E_m\langle\psi_m|\dot{\psi_n}\rangle$. Then the above equation for $n \neq m$ becomes,

$$\langle\psi_m|\dot{H}|\psi_n\rangle = (E_n - E_m)\langle\psi_m|\dot{\psi_n}\rangle \tag{1.11}$$

Substituting the above term into Eq. 1.9 gives,

$$\dot{c_m}(t) = -c_m\langle\psi_m|\dot{\psi_m}\rangle - \sum_{n\neq m} c_n\frac{\langle\psi_m|\dot{H}|\psi_n\rangle}{E_n - E_m}e^{-\frac{1}{\hbar}\int_0^t [E_n(t') - E_m(t')]dt'} \tag{1.12}$$

Now we introduce the adiabatic approximation. Assume that $\dot{H}$ is extremely small, this makes the second term negligible. This leaves us with,

$$\dot{c_m}(t) = -c_m\langle\psi_m|\dot{\psi_m}\rangle \tag{1.13}$$

which has the solution,

$$c_m(t) = -c_m(0)e^{i\gamma_m(t)} \tag{1.14}$$

where,

$$\gamma_m(t) = i\int_0^t \left\langle\psi_m(t')\right|\frac{\partial}{\partial t'}\psi_m(t')\Big\rangle dt' \tag{1.15}$$

Thus if the particle starts at the n^{th} state (this makes $c_n(0) = 1$ and $c_m(0) = 0$ for $m \neq n$), Eq. 1.4 becomes

$$\Psi_n(t) = e^{i\theta_n(t)} e^{i\gamma_n(t)} \psi_n(t) \tag{1.16}$$

The additional phase $\gamma_n(t)$ is the *geometric phase*.

1.1.4 Impact of Geometric Phase - An Example

A general notion in quantum mechanics is that the phase of a wave function is arbitrary as physical quantities involve $|\Psi|^2$, the phase part of the wave function cancels out. But this may not be the case always. For example, consider the case shown in Fig. 1.5, a wave function Ψ_0 is split into two equal halves. One of the two halves passes through an adiabatic potential. As a result, it gains a geometric phase of Γ. Whereas the other half remains invariant. If we now combine the two waves, the total wave function would be,

$$\Psi = \frac{1}{2}\Psi_0 + \frac{1}{2}\Psi_0 e^{i\Gamma}$$

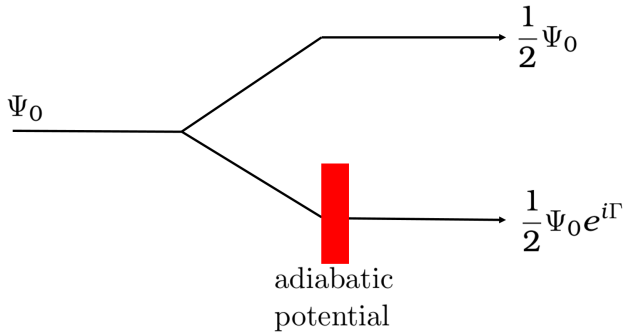

FIGURE 1.5: A wave function Ψ_0 is split into two equal halves. One of the two parts pass through an adiabatic potential and attains a phase Γ. Where as the other half remains invariant.

Then,

$$|\Psi|^2 = \frac{1}{4}|\Psi_0|^2\left(1 + e^{i\Gamma}\right)\left(1 + e^{-i\Gamma}\right)$$

$$|\Psi|^2 = |\Psi_0|^2 cos^2(\Gamma/2)$$

The above equation implies that in some situations the phase of the wave function cannot be ignored. They can play a major role.

1.1.5 Berry Phase

The eigenfunction depends on the time t becuase there is some parameter $R(t)$ in the Hamiltonian which is changing with time (such as the width of the expanding square well in the previous example). Thus we have,

$$\frac{\partial \psi_n}{\partial t} = \frac{\partial \psi_n}{\partial R}\frac{dR}{dt} \tag{1.17}$$

Then the geometric phase becomes

$$\gamma_n(t) = i\int_0^t \left\langle \psi_n \middle| \frac{\partial \psi_n}{\partial R} \right\rangle \frac{dR}{dt'} dt' = i\int_{R_i}^{R_f} \left\langle \psi_n \middle| \frac{\partial \psi_n}{\partial R} \right\rangle dR \tag{1.18}$$

where R_i and R_f are the initial and final values of $R(t)$. If the Hamiltonian returns to its initial form after time T, then $R_f = R_i$ and $\gamma_n(T) = 0$. However, if there are more than one parameter in the Hamiltonian which is changing with time,

$$\frac{\partial \psi_n}{\partial t} = \frac{\partial \psi_n}{\partial R_1}\frac{dR_1}{dt} + \frac{\partial \psi_n}{\partial R_2}\frac{dR_2}{dt} + \cdots + \frac{\partial \psi_n}{\partial R_N}\frac{dR_N}{dt} = (\nabla_R \psi_n)\cdot\frac{d\mathbf{R}}{dt} \tag{1.19}$$

This makes the geometric phase,

$$\gamma_n(t) = i\int_{\mathbf{R}_i}^{\mathbf{R}_f} \langle \psi_n | \nabla_R \psi_n \rangle \cdot d\mathbf{R} \tag{1.20}$$

Thus, if the Hamiltonian returns to its original form after time T, the total geometric phase becomes

$$\gamma_n(T) = i\oint \langle \psi_n | \nabla_R \psi_n \rangle \cdot d\mathbf{R} \tag{1.21}$$

This geometric phase is called *Berry's phase*. Berry's phase only depends on the path taken, not on how fast the path was traversed, provided the adiabatic condition is satisfied.

1.2 Berry Curvature

Applying the Stoke's theorem to the *Berry's phase*,

$$\gamma_n(T) = i \oint \langle \psi_n | \nabla_R \psi_n \rangle \cdot d\mathbf{R} = - \iint_S \Omega(\mathbf{R}) \cdot d\mathbf{S} \tag{1.22}$$

where $\Omega(\mathbf{R})$ is given by,

$$\begin{aligned} \Omega(\mathbf{R}) &= \text{Im}\, \nabla_{\mathbf{R}} \times \langle \psi_n | \nabla_{\mathbf{R}} \psi_n \rangle \\ &= \text{Im}\, \langle \nabla_{\mathbf{R}} \psi_n | \times | \nabla_{\mathbf{R}} \psi_n \rangle \\ &= \text{Im} \sum_{m \neq n} \langle \nabla_{\mathbf{R}} \psi_n | \psi_m \rangle \times \langle \psi_m | \nabla_{\mathbf{R}} \psi_n \rangle \\ &(\because \nabla \times [f \nabla g] = (\nabla f) \times (\nabla g)) \end{aligned} \tag{1.23}$$

We have already found that (Eq. 1.11),

$$\langle \psi_m | \nabla_{\mathbf{R}} H | \psi_n \rangle = (E_n - E_m) \langle \psi_m | \nabla_{\mathbf{R}} \psi_n \rangle \tag{1.24}$$

Hence we have,

$$\langle \psi_m | \nabla_{\mathbf{R}} \psi_n \rangle = \frac{\langle \psi_m | \nabla_{\mathbf{R}} H | \psi_n \rangle}{(E_n - E_m)}, m \neq n \tag{1.25}$$

Therefore Eq. 1.23 becomes,

$$\Omega(\mathbf{R}) = \text{Im} \sum_{m \neq n} \frac{\langle \psi_n | \nabla_{\mathbf{R}} H | \psi_m \rangle \times \langle \psi_m | \nabla_{\mathbf{R}} H | \psi_n \rangle}{(E_m - E_n)^2} \tag{1.26}$$

The above derived quantity $\Omega(\mathbf{R})$ is called the *Berry curvature*. Berry curvature is the physical quantity that is manipulated and controlled in order to address the carriers in valleytronics. This is in analogy to spin in spintronics. However, the material has to be satisfied with certain symmetry considerations in order to be classified as a valleytronic material. Under time reversal symmetry the Berry curvature follows the relation

$$\Omega_n(\mathbf{k}) = -\Omega_n(\textbf{-k}) \tag{1.27}$$

whereas under spatial inversion symmetry the Berry curvature follows the relation,

$$\Omega_n(\mathbf{k}) = \Omega_n(\textbf{-k}) \tag{1.28}$$

Thus if a system has both time reversal symmetry as well as the spatial inversion symmetry the Berry curvature is zero. Thus for a valleytronic material, either of the symmetry has to be broken in order to have a non-zero Berry curvature. Fig. 1.6 shows the band structure as well as the Berry curvature of single layer MoS_2. MoS_2 has a layer of Mo atom sandwiched between two layers of S atoms (shown in the inset of the top panel of Fig. 1.6). Thus the system has inherent inversion asymmetry. Thus it shows a non-zero Berry curvature at K and K′ high symmetry points with opposite polarity.

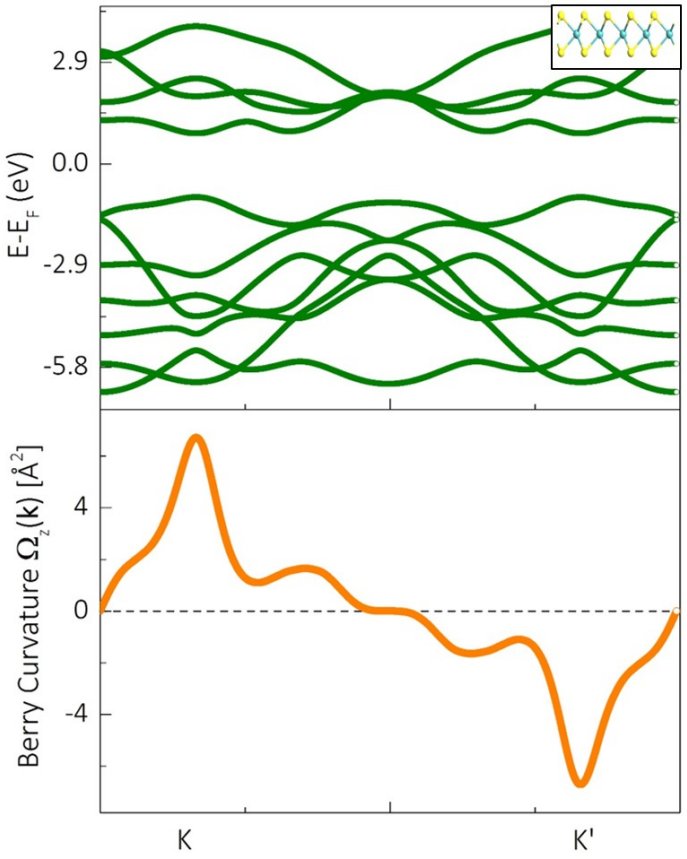

FIGURE 1.6: Top panel: Band structure of MoS_2 (Inset: Crystal structure of MoS2). Bottom panel: Berry curvature of MoS_2 with non-zero values at K and K′ highy symmetry points with opposite polarity.

1.3 Valley Hall Effect

The presence of a non-zero Berry curvature results in an anomalous velocity in the presence of an in-plane electric field (Eq. 1.28).

$$v_n(\mathbf{k}) = \frac{1}{\hbar}\frac{\partial \epsilon_n(\mathbf{k})}{\partial \mathbf{k}} - \frac{e}{\hbar}\mathbf{E} \times \Omega_n(\mathbf{k}) \tag{1.29}$$

The last term in the anomalous velocity equation is a cross product between electric field and Berry curvature. Hence the presence of non-zero Berry curvature with opposite polarity at the K and K′ valleys will force the charge carriers to move to the opposite edges of the sample in the presence of an in-plane electric field. This phenomenon is called *valley Hall effect*. Fig. 1.7 shows the schematic illustration of the valley Hall effect where charge carriers at K and K′ valleys move to the opposite edges of the material in the presence of an in-plane electric field due to the opposite Berry curvature at the two valleys.

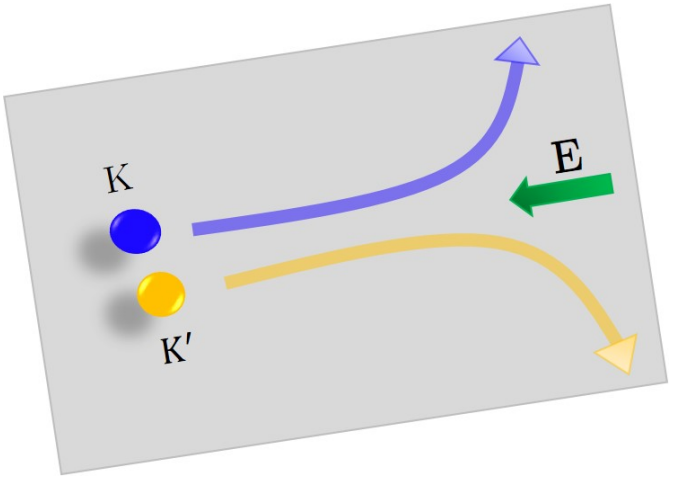

FIGURE 1.7: Schematic illustration of the valley Hall effect where charge carriers at K and K′ valleys move to the opposite edges of the material in the presence of an in-plane electric field due to the opposite Berry curvature at the two valleys.

1.4 Early Work and Motivation

Valley Hall effect in bilayer graphene-based heterostructures have been observed in recent years [42, 43]. Fig. 1.8a shows the optical micrograph of the device used for the study in reference [42]. The schematic representation of the device (Fig. 1.8b) shows bilayer graphene sandwiched between two hBN layers. They performed the non-local resistance measurement method (please refer to section 3.3 for the details on non-local measurement method) to detect valley Hall effect in the device and it is compared with the local resistance measurement. However, they could not observe any non-local signal in ungated samples (Fig. 1.8c). Non-local characteristics could only be observed once the gate voltage is applied across the heterostructure, which breaks the symmetry between the layers. Fig. 1.9 shows the non-local resistance measured at various gate voltages applied across the hBN/bilayer graphene/hBN heterostructure. Shimazaki *et al.*, [43] have also studied valley Hall effect in similar heterostructure and obtained similar results. However, some of the fundamental issues are not addressed in these studies.

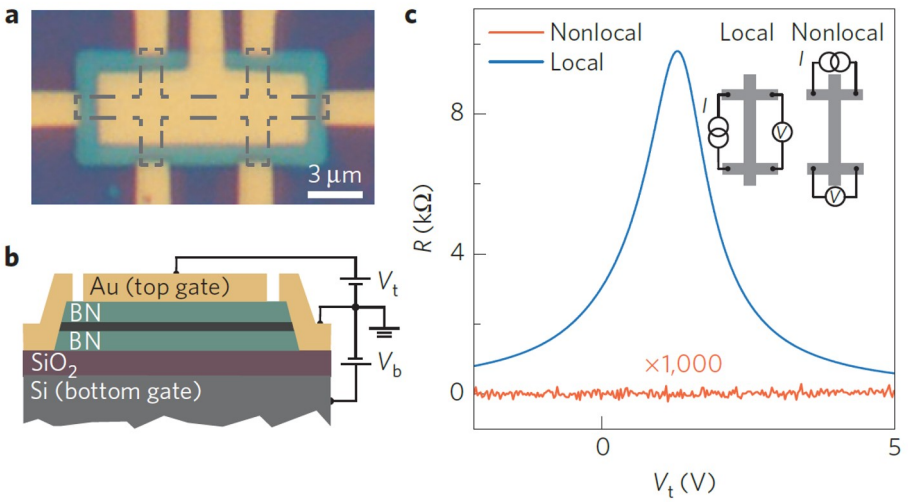

FIGURE 1.8: **a** Optical micrograph of the heterostructure. **b**schematic representation of the device. **c** The measured local and non-local resistances for the device under zero gate voltage. Image taken from [42].

One, there have been several theoretical studies [34–36] and experimental observations [38–40] arguing about an inherent asymmetry persistent in ungated bilayer graphene due to electron-electron interaction at low temperatures. Asymmetry induces Berry curvature and hence valley Hall effect. Yet, no non-local resistance was observed in the ungated samples in the above studies. Second, the effect of the presence of hBN layers at the top and bottom is not considered in these studies. Thus in our study, we try to understand these issues from a theoretical point of view.

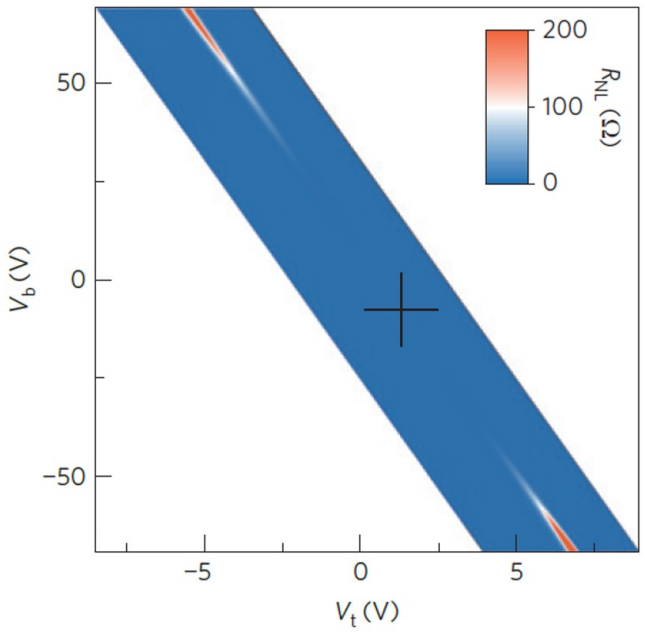

FIGURE 1.9: The measured local and non-local resistances for the device under various gate voltages applied across the device. Image taken from [42].

From an experimental point of view, the above-mentioned studies used a complicated device structure, which includes sandwiching the bilayer graphene with hBN layers and applying a gate voltage to break the symmetry between the layers. However, the presence of a substrate can also induce asymmetry between the layers of bilayer graphene due to proximity effect. This can open up a band gap and induce Berry curvature and hence valley Hall effect even under zero gate voltage. Thus we also conduct experimental studies on ungated bilayer graphene exfoliated on Si/SiO_2 substrate to study valley Hall effect.

Chapter 2

Density Functional Theory

The fundamental basis for the study of condensed matter physics and the study of materials is the understanding of the behavior of electrons in an atom or a molecule at varied conditions. The electrical, optical and magnetic properties of a material rely on the way the electron act itself in the material. But the study of a system with many electrons and nuclei could be difficult as we have to consider several interactions in the system. Thus, reasonable approximations are made to reduce the computational cost and yet obtain comparable results to that of all electron models. There is always a tradeoff between the accuracy of the results and the approximations made. However, some of the approximate theories can explain certain properties with a great amount of accuracy. In this chapter we look at some of the methods employed in this work.

2.1 Free Electron Model

The properties of an electron in a material is studied by solving the Schrödinger equation given by,

$$\left[-\frac{\hbar^2}{2m}\nabla^2 + V(\vec{r}) \right] \psi(\vec{r}) = E\psi(\vec{r}) \tag{2.1}$$

where, $\psi(\mathbf{r})$ and E are the eigenfunction and energy of the electron respectively. $V(\mathbf{r})$ represents the potential experienced by the electron, which includes the interaction of the electron with all the nuclei as well as all other electrons present in the solid. But, solving Schrödinger equation by including all these details is a mammoth, time-consuming process, although it can give results comparable to that of experiments. Thus we make appropriate approximations. Free electron model is the simplest approximation made,

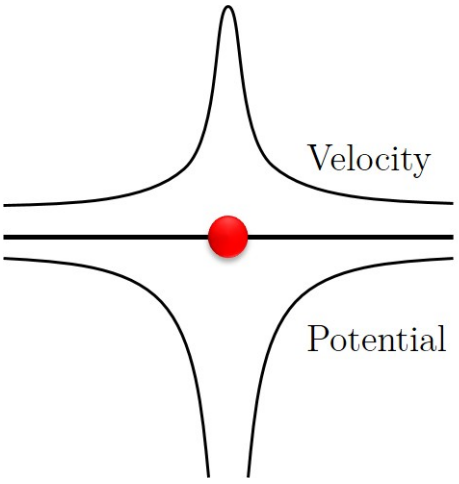

FIGURE 2.1: Schematic diagram showing the velocity of the electron in the vicinity of the ions where it has stong potential.

where we assume that the crystal potential is exactly zero so that the electron behave as free particles. In other words $V(\mathbf{r}) = 0$. Although the interaction of the electron with the ions and other electrons is neglected in this model, the free electron model works because of the following reasons. One, the Coulomb interaction of the electron with the ion is canceled by an additional repulsive potential due to quantum effects. Another way to look at it is when the electrons are at the vicinity of the ions, where it experience strong potential, the velocity of the electron increases (Fig. 2.1). Effectively it spends most of its time far away from the ions, behaving like a free electron. Second, the interaction of the electrons among themselves are also weak due to the following reason. Electrons with parallel spin stay away from each other due to Pauli exclusion principle. On the other hand, electrons with opposite spin stay away from each other in order to minimize the energy of the system.

A better approximation is the *nearly free electron* model where a weak crystal potential is taken into account through quantum mechanical perturbation method. This method introduces gaps in the band structure of the materials which are otherwise closed in the free electron model. Also, the gap which arises due to the turning on of the crystal potential occurs at the boundaries of the Brillouin zone.

2.2 Tight Binding Model

Another widely used approximate method is the tight binding model in which the ionic potential is treated as strong. Thus, when the electron is in the vicinity of an ion, the electrons remain there for a longer period of time before moving to the next ion. This implies that the electron effectively orbits around a single ion, resulting in an

atomic orbital. The electron is essentially unaffected by the neighboring ions. In other words, the electron is *tightly bound* to its own atom. However, the orbital is slightly modified by the neighboring atoms. Consider a system with n atomic orbitals $\phi_j(\mathbf{k,r})$ where, $j = 1...n$. The model can be written in terms of the atomic orbitals using n Bloch function as

$$\Phi_j(\mathbf{k,r}) = \frac{1}{\sqrt{N}} \sum_{i=1}^{N} e^{i\mathbf{k,r}_{j,i}} \phi_j(\mathbf{r\text{-}R}_{j,i})$$

where, $i = 1...N$ represents N different unit cells. The electronic wave function is the superposition of n different Bloch functions, and is given by

$$\Psi_j(\mathbf{k,r}) = \sum_{l=1}^{n} c_{j,l}(\mathbf{k}) \phi_l(\mathbf{k,r})$$

where $c_{j,l}$ is coefficient of expansion. The energy of the j^{th} band is given by

$$E_j(\mathbf{k}) = \frac{\langle \Psi_j | \, \mathcal{H} \, | \Psi_j \rangle}{\langle \Psi_j | \Psi_j \rangle}$$

where $\mathcal{H}$ is the Hamiltonian. Expanding the wave function gives

$$E_j(\mathbf{k}) = \frac{\sum_{i,l}^{n} c_{ji}^{\star} c_{jl} \langle \Phi_i | \mathcal{H} | \Phi_l \rangle}{\sum_{i,l}^{n} c_{ji}^{\star} c_{jl} \langle \Phi_i | \Phi_l \rangle}$$

$$= \frac{\sum_{i,l}^{n} H_{il} c_{ji}^{\star} c_{jl}}{\sum_{i,l}^{n} S_{il} c_{ji}^{\star} c_{jl}}$$

where $H_{il} = \langle \Phi_i | \mathcal{H} | \Phi_l \rangle$ is the transfer integral matrix element and $S_{il} = \langle \Phi_i | \Phi_l \rangle$ is the overlap integral matrix element. Minimizing the energy E_j with respect to the coefficient $c_{jm}^{\star}$ gives

$$\sum_{l=1}^{n} H_{ml} c_{jl} = E_j \sum_{l=1}^{n} S_{ml} c_{jl}$$

The above equation can be written as a matrix equation with ψ_j as the column vector.

$$H\psi_j = E_j S \psi_j$$

The energy E_j can be obtained by solving the secular equation (provided the transfer integral matrix and overlap integral matrix is known)

$$|H - E_j S| = 0$$

2.3 Hartree-Fock Method

For a many-body system consisting of electrons and nuclei, the Hamiltonian can be written as

$$\hat{H} = -\frac{\hbar^2}{2m_e}\sum_i \nabla_i^2 - \sum_{i,I}\frac{Z_I e^2}{|\vec{r_i} - \vec{R_I}|} + \frac{1}{2}\sum_{i\neq j}\frac{e^2}{|\vec{r_i} - \vec{r_j}|} - \frac{\hbar^2}{2M_I}\sum_I \nabla_I^2 \tag{2.2}$$

where each term can be explained as,

$$-\frac{\hbar^2}{2m_e}\sum_i \nabla_i^2 \Longrightarrow \text{Kinetic energy term for the electrons.}$$

$$-\sum_{i,I}\frac{Z_I e^2}{|\vec{r_i} - \vec{R_I}|} \Longrightarrow \text{Potential acting on the electron due to the nuclei.}$$

$$\frac{1}{2}\sum_{i\neq j}\frac{e^2}{|\vec{r_i} - \vec{r_j}|} \Longrightarrow \text{Electron-electron interaction.}$$

$$-\frac{\hbar^2}{2M_I}\sum_I \nabla_I^2 \Longrightarrow \text{Kinetic energy of the nuclei.}$$

As can be noted in the above terms, i and I subscripts run for electrons and nuclei respectively. m_e is the mass of the electron and M_I is the mass of the nucleus. Note that the kinetic energy term for the nucleus has the mass of the nucleus in the denominator. Since the mass of the nucleus is much higher than that of the electron ($\frac{m_p}{m_e} \approx 1836$), this term has only a minor contribution to the total energy of the system. Thus, this term can be neglected. This approximation is called Born-Oppenheimer or adiabatic approximation. Thus the Hamiltonian without the nuclear kinetic energy term becomes,

$$\hat{H} = -\frac{\hbar^2}{2m_e}\sum_i \nabla_i^2 - \sum_{i,I}\frac{Z_I e^2}{|\vec{r_i} - \vec{R_I}|} + \frac{1}{2}\sum_{i\neq j}\frac{e^2}{|\vec{r_i} - \vec{r_j}|} \tag{2.3}$$

The difficulty in soving the Schrödinger equation (Eq. 2.1) using the above Hamiltonian arises from the Coulomb interaction term ($\frac{1}{2}\sum_{i\neq j}\frac{e^2}{|\vec{r_i}-\vec{r_j}|}$). In 1928 Hartree came up with the notion of effective electron-electron potential ($V_{eff}(\vec{r}) = \int d\vec{r}\frac{e^2 n(\vec{r})}{|\vec{r_i}-\vec{r_j}|}$) i.e. every electron moves in an effective potential produced by sum of all other electrons. The

Hamiltonian with effective potential term instead of the Coulomb term is called the Hartree equation. A major drawback of the Hartree equation was that it does not incorporate Pauli exclusion principle. Thus Fock and Slater formulated an antisymmetric wave fuction in order to include Pauli exclusion principle. The wave function inclusive of the spin is given by

$$\psi_i(\vec{r}) = \phi_i(\vec{r_i})\alpha_i \tag{2.4}$$

where, $\phi_i(\vec{r_i})$ is orbital part and α_i is the spin part. The hamiltonian is given by,

$$\hat{H} = -\frac{\hbar^2}{2m_e}\sum_i \nabla_i^2 - \sum_{i,I}\frac{Z_I e^2}{|\vec{r_i} - \vec{R_I}|} + J_{ij} - K_{ij} \tag{2.5}$$

where

$$J_{ij} = \frac{1}{2}\int d\vec{r_i} d\vec{r_j} \sum_{i,j,\alpha_1,\alpha_2} \frac{e^2}{|\vec{r_i} - \vec{r_j}|}|\psi_i(1)|^2|\psi_j(2)|^2 \tag{2.6}$$

is the *Coloumb integral* and

$$K_{ij} = \frac{1}{2}\int d\vec{r_i} d\vec{r_j} \sum_{i,j,\alpha_1,\alpha_2} \frac{e^2}{|\vec{r_i} - \vec{r_j}|}\psi_i^\star(1)\psi_j^\star(2)\psi_i(2)\psi_j(1) \tag{2.7}$$

is the *exchange integral*. The Coulomb integral takes care of the potential energy interaction between i^{th} electron and the j^{th} electron. On the other hand, exchange integral which does not have a classical analog arises from the necessity that the wave function should be antisymmetric with respect to electron exchange. The Hartree-Fock equations are solved using an iterative method known as the self-consistent field (SCF) method. As per this method, a most probable form of the orbital is taken as an initial guess. This orbital is improved with each iteration until the energy reaches a minimum and the orbitals no longer change.

Although the Hartree-Fock method was successful in computing many electronic properties, it failed to address one important aspect of the electronic interaction which is *correlation*. The electrons are not independent of each other as assumed by the Hartree-Fock method, rather they are correlated to each other so as to minimize the energy.

2.4 Density Functional Theory

The underlying idea of the density functional theory is that the electron density contains all the information incorporated in a many-body wave function. This was observed by Hohenberg and Kohn in 1964. They pointed out that if the density of the electron in the ground state is known, then one can deduce the external potential in which the electron resides. The electronic density at a point $\vec{r}$ in space is given by

$$n(\vec{r}) = N \int d\vec{r}_1 ... d\vec{r}_N \Psi^\star(\vec{r}_1, \vec{r}_2 ... \vec{r}_N) \delta(\vec{r} - \vec{r}_1) \Psi(\vec{r}_1, \vec{r}_2 ... \vec{r}_N) \tag{2.8}$$

All the solid systems have electrons moving in a potential V, with kinetic energy T, interacting with each other by Coulomb potential V_{ee}. As per the underlying idea of the density functional theory, if the charge density is given, all the above parameters and the ground state energy can be written as the functional of the density. In other words,

$$E[n] = T[n] + V[n] + V_{ee}[n] \tag{2.9}$$

here the density n is a function of space ($n(\vec{r})$). The energy functional (Eq. 2.9) can also be written as

$$E[n] = \int d\vec{r} n(\vec{r}) V(\vec{r}) + F[n] \tag{2.10}$$

where $F[n]$ is the sum of kinetic energy and Coloumb energy, i.e.,

$$F[n] = T[n] + V_{ee}[n] \tag{2.11}$$

The functional F does not depend on the potential V and it also does not depend on what kind of system we have. Thus the functional F is an universal functional for all systems of N particles. If this magical functional could be found once and for all, it can solve many-body problems for all external potentials V. However, a true F does not exist and never will be. Hence various approximations are made for the functional F, which best represents the known results such as the *Thomas-Fermi-(Dirac) equations* and the *Kohn-Sham equations*.

2.4.1 Thomas-Fermi-(Dirac) Equations

Thomas and Fermi gave the simplest approximation for the functional *F[n]* and hence *E[n]*. The idea here is to find the energy of the electron as a function of electron density in a spatially uniform density. Unfortunately, the Coloumb interactions cannot be solved in a uniform potential exactly except at high charge density. Thus Hartree-Fock approximation is used to obtain all the terms in the Schrödinger equation which cannot be expressed in terms of the charge density. Two terms evaluated this way is the kinetic energy term and the exchange energy term. Thus in the Thomas-Fermi theory, which assumes that the charge density is not uniform, but varies slowly, the kinetic energy term and the exchange energy term are evaluated locally and integrated over all space. The kinetic energy term is expressed as

$$T[n] = \int d\vec{r} \frac{\hbar^2}{2m} \frac{3}{5} (3\pi^2)^{2/3} n^{5/3}(\vec{r}) \tag{2.12}$$

and the exchange energy term is given by

$$E_{xc} = -\int d\vec{r} \frac{3}{4} \left(\frac{3}{\pi}\right)^{1/3} e^2 n^{4/3}(\vec{r}) \tag{2.13}$$

The potential and the Coloumb terms are expressed as a functional of the density. Thus, combining all the terms, the density functional is given as,

$$E[n] = \int d\vec{r} \frac{\hbar^2}{2m} \frac{3}{5} (3\pi^2)^{2/3} n^{5/3}(\vec{r}) + \int d\vec{r} n(\vec{r}) V(\vec{r}) + \frac{1}{2} \int d\vec{r}_2 d\vec{r}_1 \frac{e^2 n(\vec{r}_1) n(\vec{r}_2)}{|\vec{r}_1 - \vec{r}_2|} - \int d\vec{r} \frac{3}{4} \left(\frac{3}{\pi}\right)^{1/3} e^2 n^{4/3}(\vec{r}) \tag{2.14}$$

The above equation with the last term (exchange term) omitted is the *Thomas-Fermi equation* whereas the functional including the exchange term is called the *Thomas-Fermi-Dirac equation.*

2.4.2 Kohn-Sham Equations

The Kohn-Sham Equations are widely used to solve the properties of many electron systems. In this method, instead of writing all the material properties as a function of electron density, they considered N single electron wave functions $\psi_i(\vec{r})$ and obtained the charge density from them by,

$$n(\vec{r}) = \sum_{i=1}^{N} |\psi_i(\vec{r})|^2 \tag{2.15}$$

The kinetic energy term as a functional of density is given by,

$$T[n] = \sum_i \frac{\hbar^2}{2m} \int d\vec{r} \quad |\nabla \psi_i(\vec{r})|^2 \tag{2.16}$$

Now, instead of varying with respect to the charge density we vary with respect to the wave function because we know the density as a function of the wave function, however, the reverse is not true (we do not know the wave function as a function of the charge density). The Schrödinger equation varying with respect to the wave function is given by

$$-\frac{\hbar^2}{2m}\nabla^2\psi_i(\vec{r}) + \left[V(\vec{r}) + \int d\vec{r}' \frac{e^2 n(\vec{r}')}{|\vec{r} - \vec{r}'|} + \frac{\delta E_{xc}(n)}{\delta n}\right]\psi_i(\vec{r}) = E_i\psi_i(\vec{r}) \tag{2.17}$$

2.4.2.1 Local Density Approximation (LDA)

The above approximation (Eq. 2.17) is called the *Local Density Approximation* (LDA). The essential idea of the approximation is as follows. The potential due to the exchange term is given by

$$V_{xc} \equiv \frac{\delta E_{xc}(n)}{\delta n} \tag{2.18}$$

The LDA is an approximation to this unknown term. In reality the potential acting on a point depends on the density of all other points. However, LDA approximate that the potential depends only on the density of the density at that point and this is done for all the points. Thus the potential due to the exchange term (V_{xc}) which was a functional of the density, becomes a function of the density. In other words,

$$V_{xc}[n](\vec{r}) \approx V_{xc}(n(\vec{r})) \tag{2.19}$$

2.4.2.2 Generalized Gradient Approximation (GGA)

Several other approximations also exist as a consequence of the effort to make the results close to the experiment such as the *Generalized Gradient Approximations* (GGA). Here the approximation is that the density at a point not only depends on the

denity at that point, but also its derivative at that point and higher derivatives. That is,

$$V_{xc}[n](\vec{r}) \approx V_{xc}(n(\vec{r}), \vec{\nabla} n(\vec{r})) \tag{2.20}$$

Now, in DFT also the solution is obtained by self-consistency method. The potential depends on the solution which is the density. We need to know the wave function to know the density and the density defines the potential. This is solved iteratively using self-consistency. We start with a guess density, obtain the potential, then solve the problem. Once the problem is solved we get a wave function and use this wave function to get the new density. This process is continued until the input density and the output density are sufficiently equal.

2.4.3 K-point Sampling

In periodic solid the electronic states are labeled by the k-vector along with the band index. Finding the density involves the integral of the square of the occupied wave functions which are labeled by band index and k-vector. This integration which runs over all the Brillouin zone is approximated as the sums over selected k-points. This is called Brillouin zone sampling or k-point sampling. The accuracy of the results greatly depends on the Brillouin zone sampling i.e, the number of k points selected as well as the position of the selected k points in the Brillouin zone. The computational cost increases with the number of k points. Thus, the appropriate number of k points is identified by testing the convergence of the calculation. Over the years, different k point sampling methods have been implemented and tested such as *mean value point* (where just one point is used to calculate the required quantity) and *special k-points* (where few points are selected to give fast convergence). But these were used in the olden days when computing was not so efficient. When computing efficiency got improved, more accurate methods took over such as *Monkhorst-Pack method*.

In this method, the reciprocal lattice primitive unit cell is divided into $N_1 \times N_2 \times N_3$ points with each point having equal weights. Fig. 2.2 shows an example of k-point sampling in the reciprocal lattice with a *Monkhorst-Pack* grid of $4 \times 4 \times 1$. The accuracy of the calculation as well as the computational cost increases with the number of k-points. Thus, the convergence test is necessary to determine the level of accuracy.

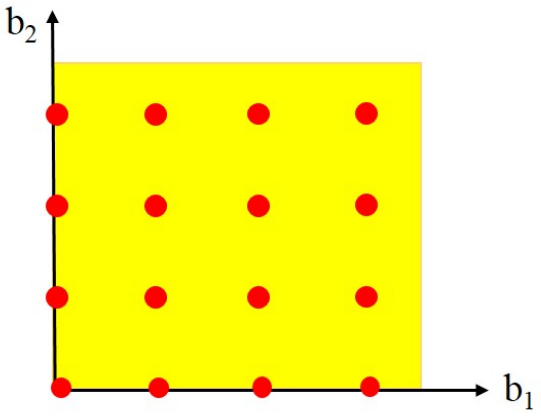

FIGURE 2.2: Schematic representation of k-point sampling in the resiprocal lattice. The Monkhorst-Pack grid shown is $4 \times 4 \times 1$.

2.4.4 Pseudopotentials

The electrons of an atom can be distinguished as core electrons and valence electrons. The core electrons which are tightly bound to the nucleus respond very little to the presence of neighboring atoms. They are trapped in the deep potential of the nucleus. On the other hand, the valence electrons are which are in a smooth potential of the nucleus are affected by the changes happening in its surroundings. If we consider the energy eigenvalue of these electrons, the core electrons are much deeper in energy compared to the valence electrons. These observations imply that the core electrons are chemically inert. In other words, only the valence electrons are involved in chemical bonding. In terms of the computation of physical and chemical parameters, the core electrons make the calculation more expensive as we have to deal with more electrons. The main role of the core electrons is to screen the nuclear potential seen by the valence electrons. The above facts lead to the idea of *Pseudopotentials*. The idea is to ignore the dynamics of the core electrons and replace their effect by an effective potential, which is the *Pseudopotentials*.

2.5 Wannier Functions

Wannier functions are set of orthonormal wave functions which are highly localized around the atomic sites. Wannier functions can be easily constructed from Bloch funtions. Wannier functions for the electrons in the n^{th} band which are centered at the lattice site R is expressed as,

$$\mathcal{W}_n(\vec{R},\vec{r}) = \frac{1}{\sqrt{N}} \sum_{\vec{k}} e^{-\vec{k}\cdot\vec{R}} \psi_{n\vec{k}}(\vec{r}) \tag{2.21}$$

These functions being orthonormal and highly localized, are employed in the calculations which use atomic orbitals. Many physical phenomena involve spatially localized objects such as impurities, crystal defects, excitons, polarons. Thus, expressing the interactions in terms of the localized orbitals reduces the complexity of the problem considerably. Although the use of atomic functions rather than Bloch functions seems to be advantageous in these circumstances, the non-orthogonality of the atomic functions makes them less attractive. Here comes the importance of Wannier functions which are both orthonormal and localized.

Wannier functions are also used along with *ab initio* calculations to study the band structure and several other properties related to materials. Maximally localized Wannier functions can replicate the *ab initio* states up to the Fermi level exactly and to a great extent for the few lower conduction bands. Fig. 2.3 shows the band structure of bilayer graphene along with the high symmetry points. The solid line corresponds to the band structure obtained using the *ab initio* calculation and the dotted line corresponds to the bands obtained through the Wannier interpolation scheme. As is evident from the figure, all the occupied and two unoccupied bands constructed through the Wannier-based calculation exactly matches with the fully *ab initio* bands. Hence it can

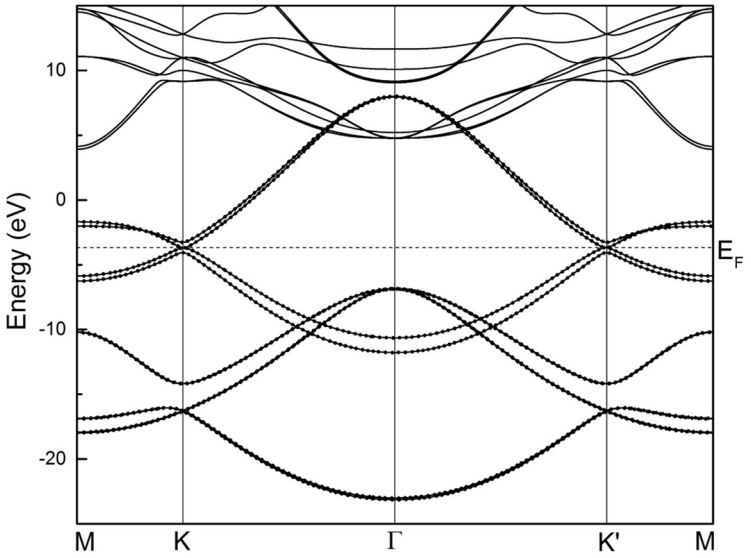

FIGURE 2.3: Band structure of bilayer graphene through the high symmetry points. Solid lines : band structure evaluated using *ab initio* method. Dotted lines: band structure obtained by Wannier interpolation scheme. Both the plots exactly matches for all the occupied bands and two un-occupied bands. The horizontal dotted line denotes the Fermi level.

be presumed that the Wannier based evaluation of physical properties such as Berry curvature and orbital magnetization, which is related to the occupied manifold should have a perfect agreement to that of *ab initio* calculation.

2.5.1 Berry Curvature Calculation Using Wannier Functions

Berry curvature for the nth band is defined as

$$\mathbf{\Omega}_n(\mathbf{k}) = i\boldsymbol{\nabla} \times \langle u_{n\mathbf{k}} | \, \boldsymbol{\nabla}_{\mathbf{k}} \, | u_{n\mathbf{k}} \rangle \tag{2.22}$$

where $\mathbf{A}_n(\mathbf{k}) = i \langle u_{n\mathbf{k}} | \, \boldsymbol{\nabla}_{\mathbf{k}} \, | u_{n\mathbf{k}} \rangle$ is the Berry connection and $|u_{n\mathbf{k}}\rangle$ is the periodic part of the Bloch function for the nth band. The summation runs over all the bands including the unoccupied bands. The total Berry curvature is the sum over all the occupied bands, i.e.,

$$\mathbf{\Omega}(\mathbf{k}) = \sum_n f_n \mathbf{\Omega}_n(\mathbf{k}) \tag{2.23}$$

where f_n is the Fermi-Dirac distribution.

But taking the derivative of the periodic part of the Bloch function (Eq. 2.22) makes the calculation cumbersome. Thus we rely on the more accurate Wannier interpolation scheme, where the Berry curvature is calculated in terms of the Wannier functions (Eq. 2.21) [21] using finite differences. The approach begins by creating Wannier functions for all the occupied states and a few un-occupied states. In the present calculation, we have considered two un-occupied states above the Fermi level. Subsequently, the Wannier space Hamiltonian is constructed by fitting the first principle band dispersion. Following the conventions of Ref. [21], Hamiltonian in the Wannier basis is given by

$$H^{(W)}_{nm}(\mathbf{k}) = \langle u^{(W)}_{n\mathbf{k}} | \, \hat{H}(\mathbf{k}) \, | u^{(W)}_{n\mathbf{k}} \rangle \tag{2.24}$$

Diagonalizing the above Hamiltonian using a suitable unitary rotation matrix yields the eigenvalues which replicate the true first principle eigenvalues. i.e.,$H^{(H)}_{nm}(\mathbf{k}) = \varepsilon^{(H)}_{n\mathbf{k}} \delta_{nm}$ and $\varepsilon^{(H)}_{n\mathbf{k}} = \varepsilon_{n\mathbf{k}}$. Corresponding Bloch states are given by

$$|u^{(H)}_{n\mathbf{k}}\rangle = \sum_m |u^{(W)}_{m\mathbf{k}}\rangle \, U_{mn}(\mathbf{k}) \tag{2.25}$$

Now the Berry curvature in terms of the above bases is given by

$$\mathbf{\Omega}(\mathbf{k}) = \sum_n f_n \overline{\mathbf{\Omega}}^H_{nn} + \sum_{n,m} (f_m - f_n) \mathbf{D}^H_{nm} \times \overline{\mathbf{A}}^H_{nm} + \mathbf{\Omega}^{DD} \tag{2.26}$$

where $\overline{O}^H = U^\dagger O^W U$ represent the components which transform covariently from Wannier gauge (W) to Hamiltonian gauge (H) under unitary transformation U; and $\boldsymbol{D}^H_{nm} = \frac{(U^\dagger \nabla H^W U)_{nm}}{\varepsilon_m - \varepsilon_n}(1 - \delta_{nm})$. The last term is defined as

$$\mathbf{\Omega}^{DD} = \frac{i}{2} \sum_{n,m} (f_n - f_m) \frac{(U^\dagger \nabla H^W U)_{nm} \times (U^\dagger \nabla H^W U)_{nm}}{(\varepsilon_m - \varepsilon_n)^2} \tag{2.27}$$

Here, H^W is the Hamiltonian in Wannier representation and ε_n is the energy of the n^{th} band. The summation runs over all the Wannier states [22], which is, all the occupied and two un-occupied states in this case. As for Berry curvature calculation, this scheme is more efficient compared to the previously implemented methods [23] where the summation runs over all the un-occupied states apart from the occupied ones. Hence the above formulation was used to calculate the Berry curvature in this study.

Chapter 3

Experimental Methods

3.1 Graphene

Graphene is a 2 dimensional (2D) material with single atom thickness made of carbon atoms arranged in hexagonal honeycomb structure (Fig.3.1a). Graphene was first isolated from thick graphite flake through micromechanical cleavage [14] (Fig.3.1b shows the optical image of single-layer graphene on Si/SiO_2 substrate). Since its first isolation, there have been several other 2D materials which were exfoliated from its bulk counterpart [15]. However, graphene remains the most studied 2D material because of its extraordinary properties which include excellent electronic, magnetic, thermal and optoelectronic properties [16, 17]. A peculiar feature of graphene which makes it special is the electric field effect on the conductivity (Fig. 3.2). It has bipolar conductivity which linearly increases with the increase in the gate voltage, i.e., application of positive and negative gate voltages can induce electrons and holes respectively into the graphene layer.

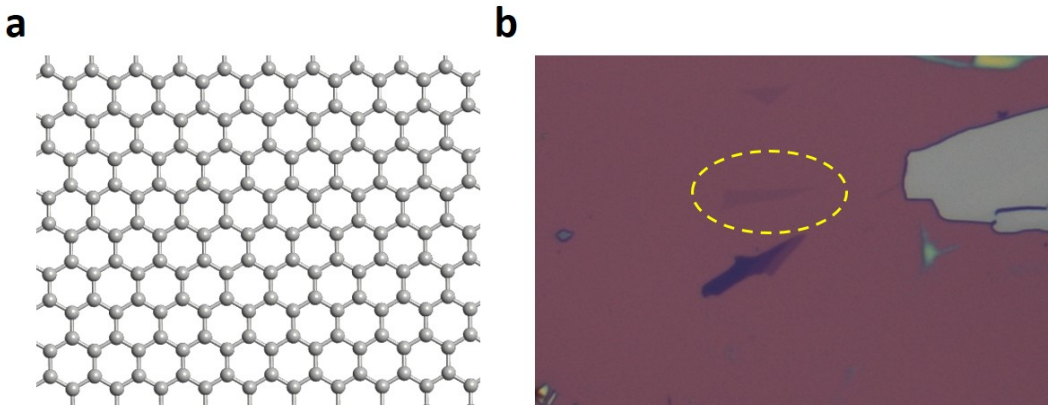

FIGURE 3.1: **a** Schematic diagram of a single layer graphene with carbon atoms arranged in hexagonal honey comb structure. **b** Optical image of a single layer graphene (inside the dotted yellow circle) exfoliated on Si/SiO_2 substrate.

For neutral graphene, the minimum conductivity (charge neutrality point) is at V_g=0. For p-doped graphene, the charge neutrality point shifts towards the positive gate voltage whereas for n-doped graphene, the charge neutrality point shifts towards the negative gate voltage. This peculiar feature makes graphene useful in various applications such as gas sensing [18], transistors [19] and also to study the fundamental physical properties [20].

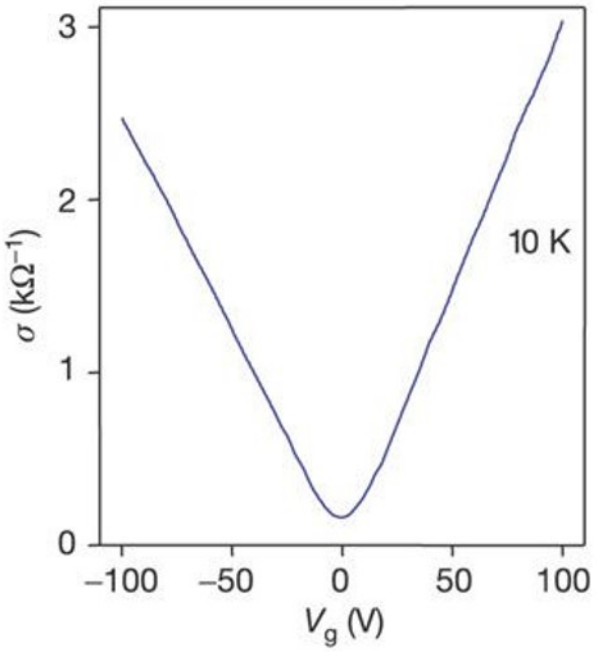

FIGURE 3.2: Gate characteristics of a single layer graphene showing the charge neutrality point at V_g=0. Application of positive and negative gate voltages can induce an appreciable amount of electrons and holes respectively into the graphene layer. Image taken from [16]

3.2 Bilayer Graphene Valleytronic Device

In this study we used bilayer graphene to study its valleytronic properties. The device fabrication process starts by exfoliating graphene on Si/SiO_2 substrate from graphite flakes using the scotch tape method. The number of layers is identified using Raman spectroscopy. The characteristic of the 2D Raman peak of the graphene layers is an indication of the number of layers. If the 2D peak could be fitted with a single Lorentzian function, the graphene is a single layer. However, 2D peaks of the graphene flakes which require four and six Lorentzian functions for a perfect fit is identified to be bilayer and trilayer graphene respectively. Fig. 3.3 shows the 2D peaks of the single layer (Fig. 3.3a), bilayer (Fig. 3.3b) and trilayer (Fig. 3.3c) graphene which are fitted with Lorentzian functions.

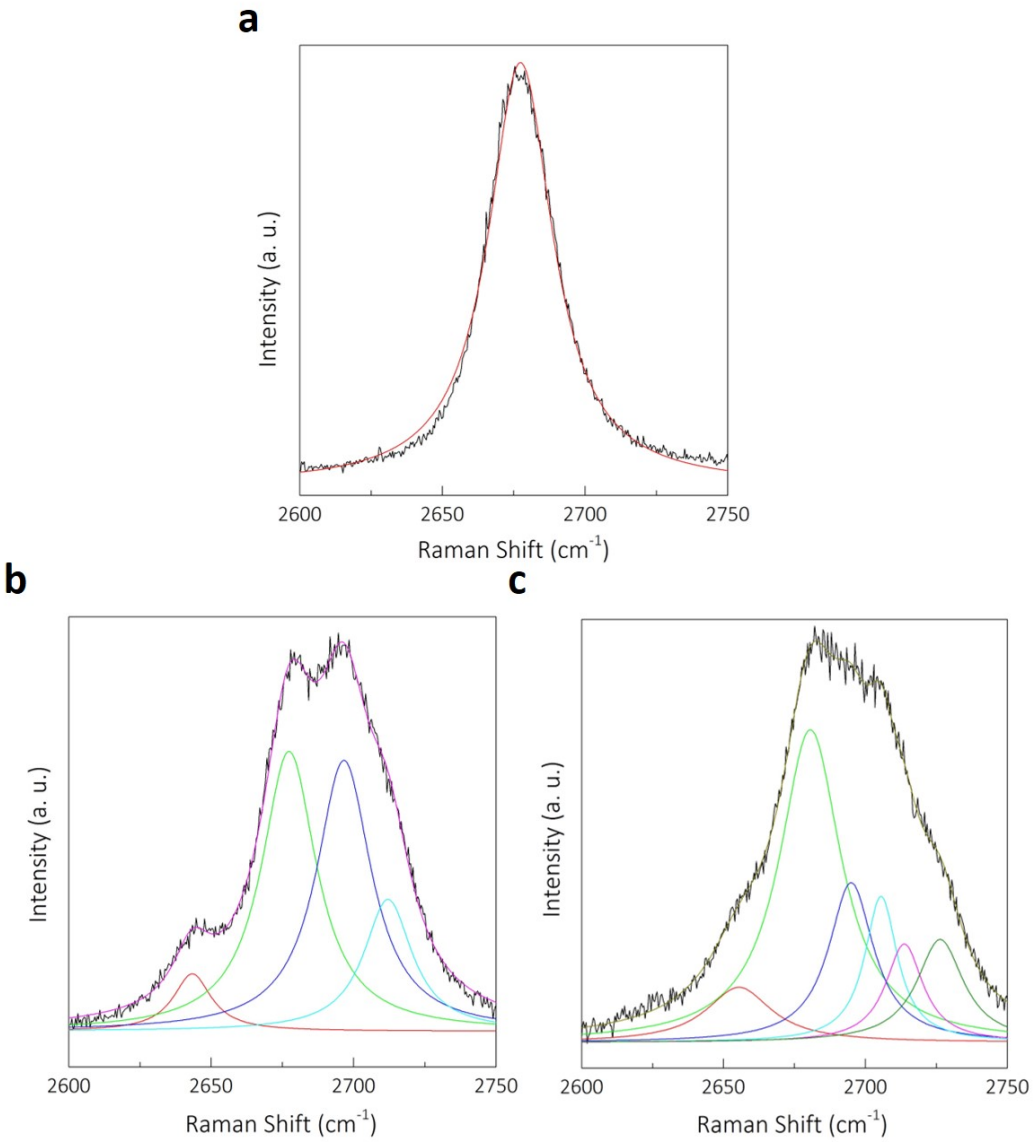

FIGURE 3.3: 2D Raman peak of **a** single layer **b** bilayer and **c** trilayer graphene fitted with Lorentzian functions

Once the bilayer graphene is identified on the Si/SiO_2 substrate, the process of making bilayer graphene device is illustrated in Fig. 3.4. Fig. 3.4a shows the schematic representation of bilayer graphene on Si/SiO_2 substrate. The Si/SiO_2/bilayer graphene is coated with MMA/PMMA resist (positive resist) in order to perform Electron beam lithography (EBL) (Fig. 3.4b). EBL makes the exposed parts of a positive resist soluble in a developer. Thus the portion where the contacts are to be made were exposed using EBL. Now, the Si/SiO_2/bilayer graphene/MMA/PMMA is put in a developer to dissolve the exposed part. The developing procedure is as follows. The Si/SiO_2/bilayer graphene/MMA/PMMA is dissolved in 1:3 IPA:MIBK solution for 51 seconds followed by pure IPA solution for 30 seconds. Fig. 3.4c shows the schematic representation of the substrate after developing. The resist at the exposed portion of the

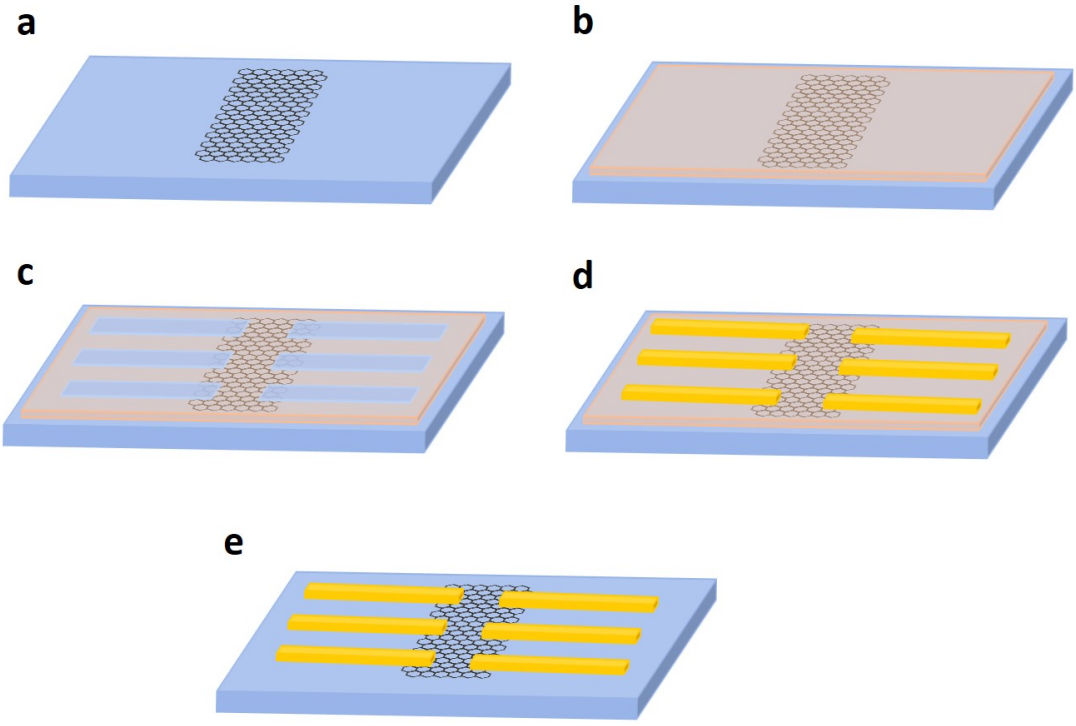

FIGURE 3.4: Schematic illustration of the fabrication process of the graphene device. **a** Bilayer graphene exfoliated on Si/SiO_2 substrate. **b** The Si/SiO_2/bilayer grphene is coated with MMA/PMMA resist (positive resist) in order to perform Electron beam lithography (EBL). **c** The EBL exposed portion of the resist is dissolved in the developer. **d** Cr/Au contacts deposited on the Si/SiO_2 substrate. **e** The final device after removing the resist by dissolving in acetone followed by IPA and DI water.

substrate is dissolved. The next step is to evaporate gold (Au) onto the Si/SiO_2/bilayer graphene/MMA/PMMA in order to make the contacts. Since the adhesion of Au on Si/SiO_2 substrate is not very good, a 10 nm thick Chromium (Cr) was evaporated onto the substrate before depositing gold. A 60 nm thick layer of gold was deposited after Chromium. Fig. 3.4d is the schematic representation of the device after gold deposition. (In reality, gold and chromium will be deposited all over the substrate after evaporation. However, the Cr/Au will be in contact with the substrate and the graphene only at those portions where the resist is not present as it is dissolved after EBL. Other parts of the substrate and the graphene are protected by resist). After evaporation of Cr/Au, the resist is removed by dissolving in acetone followed by IPA and DI water. This results in the removal of the Cr/Au which was present on the resist and only the contacts which are desired remain on the substrate (Fig. 3.4e). Fig. 3.5 shows the optical micrograph of a bilayer graphene device which is fabricated following the steps described above.

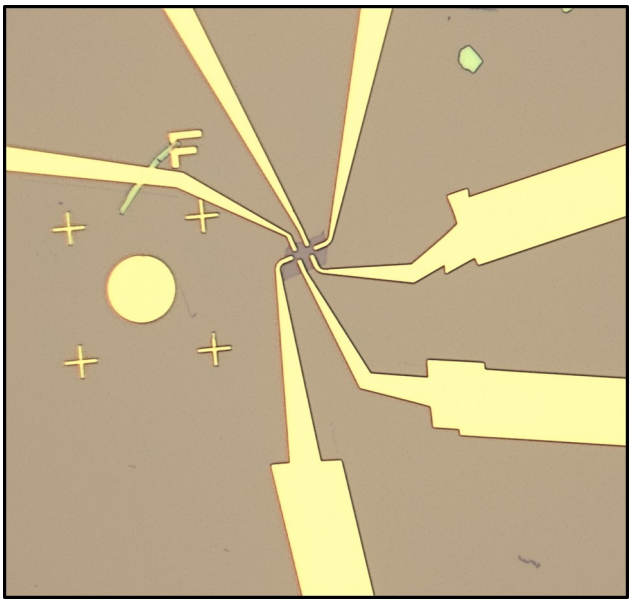

FIGURE 3.5: Optical micrograph of a bilayer graphene device. False colour is used in order to enhance the clarity.

3.3 Non-Local Electrical Measurement

Non-local electrical measurement is used to detect the valley Hall effect in bilayer graphene. Usually, the electrical properties such as the field effect characteristic are studied using the local electrical measurement, where the current is sent across the length of the device and the voltage is detected at the two ends. However, in the non-local measurement setup, the current is sent across the terminals at one end of the device and the voltage is detected at the other end. Fig. 3.6a and fig. 3.6b shows the schematic illustration of local and non-local electrical measurements respectively. In the non-local measurement, since the current is sent only across the terminals at one end, there should be some driving force which pushes the charge carriers across the length of the device to the other end. This driving force is called the Berry curvature as discussed earlier. Thus the Berry curvature can be considered as a pseudo-magnetic field in the reciprocal

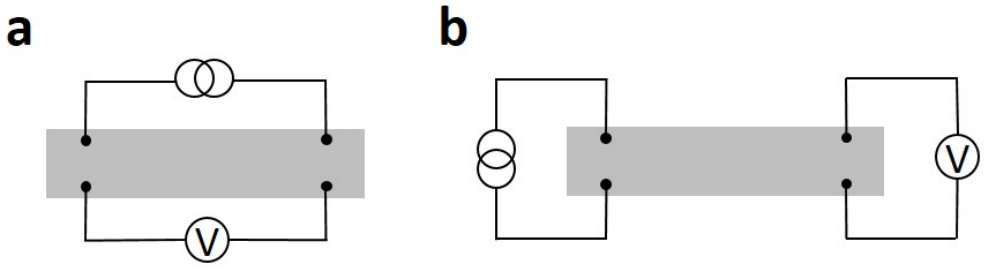

FIGURE 3.6: Schematic illustration of **a** local electrical measurement and **b** non-local electrical measurement.

lattice. Fig. 3.7 shows the local and non-local resistance measurements for a bilayer graphene device sandwiched between two hBN layers. The measurements performed at various gate voltages are also shown. As mentioned before the non-local resistance appear as a result of the valley Hall effect where the electrons in the K and K′ valleys of the bilayer graphene move to the opposite edges of the device since the Berry curvature which drives the carriers at the two valleys have opposite polarity.

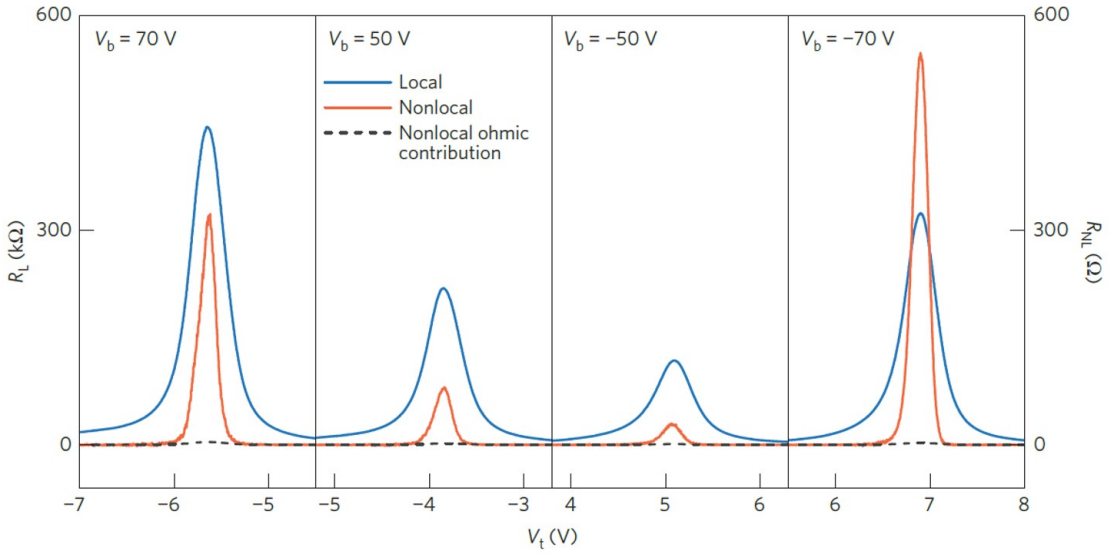

FIGURE 3.7: Local and non-local resistance measurements for a bilayer graphene device sandwiched between two hBN layers. The measurements performed at various gate voltages are also shown. Image taken from reference [42].

Chapter 4

Electrically controlled valley states in bilayer graphene

Valley current, a stable, dissipationless current, originates due to the emergence of Berry curvature in inversion symmetry broken systems. Several theoretical predictions and experimental observations have explored layer symmetry breaking in AB-stacked bilayer graphene due to long-range Coulomb interaction between the electrons. However, none of the experimental studies conducted so far have observed valley current in ungated bilayer graphene, which makes it vital to study the Berry curvature in ungated bilayer graphene. In this study, we observed a non-zero Berry curvature with opposite values at K and K′ valleys, validating the argumentation of the asymmetry persistent in ungated bilayer graphene. The magnitude, as well as the polarity of the Berry curvature, is tunable with the application of an out-of-plane electric field. These results are especially important because it can lead to the realization of a valley valve, in which the carriers from the K and K′ valleys can be regulated with a gate at the centre of the bilayer graphene nanoribbon.

4.1 Introduction

Berry phase and related phenomena have gained considerable scientific interest since its introduction[1]. It boosted the study of yet another degree of freedom in electrons i.e., valley degree of freedom and a brand new branch of research, valleytronics [2, 24, 25]. In the same way as the spin of the electron is used to manipulate and control electrons in spintronic devices, Berry curvature and orbital magnetic moment, which are two physical properties associated to the Berry phase of Bloch electrons, are utilized to manipulate electrons in valleytronics [6]. Two-dimensional materials such as graphene

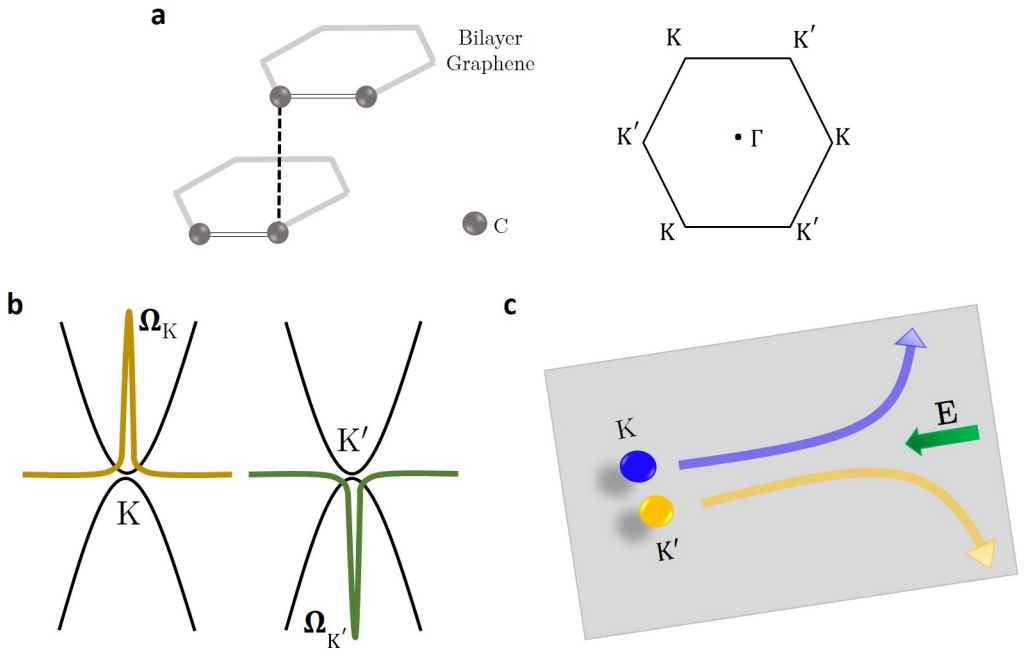

FIGURE 4.1: **a** Schematic representation of the unit cell of bilayer graphene with four carbon atoms arranged in AB stacking. The hexagonal Brillouin zone is schematically drawn with the K and K′ points at the alternate corners and the Γ point at the center. **b** A non-zero Berry curvature with opposite values at the two in-equivalent valleys at the K and K′ points of the Brillouin zone is observed in systems where inversion symmetry is broken. **c** Valley Hall effect: The presence of a non-zero Berry curvature with opposite values at K and K′ valleys drives the electrons in the two valleys towards the opposite edges of the sample in the presence of an in-plane electric field.

and Transition Metal Dichalcogenides (TMDs), which has in-equivalent valleys in their band structure at the K and K′ corners of the Brillouin zone is of particular interest to the valleytronics study, because, Berry curvature and orbital magnetic moment exhibit contrasting behaviour at these valleys (Fig. 4.1a-b) [3–5]. Berry curvature can be described as a pseudo-magnetic field in the reciprocal space which drives the carriers according to the direction of the Berry curvature. A direct consequence of which is the phenomenon Valley Hall Effect (VHE), where electrons at the two valleys drift to the opposite edges of the materials in the presence of an in-plane electric field due to the equal, but, opposite Berry curvature at the two valleys(Fig. 4.1c) [26, 27].

A prerequisite for the emergence of Berry curvature is the broken inversion symmetry or broken time-reversal symmetry [26, 28, 29]. TMDs are inversion asymmetric and are widely studied for valleytronic properties. However, the short distance between the valleys in TMDs makes them vulnerable to intervalley scattering which is not desirable in valleytronic materials. Thus, systems such as (AB-stacked) bilayer graphene which possess large intervalley distance can be an excellent candidate for valleytronics study. Also, the symmetry in (AB-stacked) bilayer graphene can be regulated

on demand using external perturbation such as electric field [30–33] (Hereafter, all the discussions are about AB-stacked bilayer graphene unless otherwise specified).

Although bilayer graphene is widely considered to be symmetric, there have been several theoretical studies [34–36] and experimental observations [38–40] arguing about an inherent asymmetry persistent in ungated bilayer graphene due to electron-electron interaction at low temperatures. Thus bilayer graphene should exhibit valley contrasting behavior even at zero electric and magnetic fields. On the light of these studies, Berry curvature due to layer polarization is anticipated in ungated bilayer graphene [41]. However, M. Sui *et al.* [42] and Y. Shimazaki *et al.* [43] who has independently studied valleytronics in bilayer graphene through non-local electrical measurement, could not observe a non-local current (valley current induced by Berry curvature) in ungated bilayer graphene. Thus in this work, we look for the existence of Berry curvature in pristine bilayer graphene and the effect of external perturbation such as out-of-plane electric field on the Berry curvature.

The *ab initio* calculations are performed within density-functional theory using the Linear Combination of Atomic Orbitals (LCAO) method implemented in the package SIESTA [48]. van der Waals exchange correlation functionals [49] were used in order to obtain the interlayer distance in close proximity to the experimental values. A vacuum layer of thickness 20 Å was used to avoid the interaction between adjacent bilayers. A fine Monkhorst-Pack grid of 36 x 36 x 1 and a mesh cut off of 400 Ry was used in all the calculations. The atomic positions are optimized until the force on each atom is less than 0.01 eV/Å. The Berry curvature calculations are performed using the Wannier90 package which follows the Wannierization procedure [50]. A total of ten Wannier functions are constructed on a fine Monkhorst-Pack grid of dimension 36 x 36 x 1. In the disentanglement procedure, the Wannier spread is converged down to 10^{-10} Å^2 in less than 600 iterations.

As for calculations performed using QUANTUM ESPRESSO [51] which uses plane wave basis, PBE exchange-correlation functional [52] which employs Generalized Gradient Approximation (GGA) is used. A norm-conserving pseudo-potential with kinetic energy cutoff for wave functions of 80 Ry is used (320 Ry for charge density cutoff). In order to procure optimum interlayer distance between the two graphene layers, semi-empirical Grimme's DFT-D2 [53] van der Waals correction is employed. The Berry curvature calculations are performed using the WANNIER90 package which follows the Wannierization procedure [50]. A total of 10 Wannier functions are constructed on a fine Monkhorst-Pack grid of dimension 72 x 72 x 1. In the disentanglement procedure, the Wannier spread is converged down to 10^{-10} Å^2 in less than 600 iterations.

4.2 Berry curvature at zero electric field

Berry curvature for the nth band is defined as

$$\mathbf{\Omega}_n(\mathbf{k}) = i\frac{\hbar^2}{m^2}\sum_{n\neq n'}\frac{\langle u_{n,\boldsymbol{k}}|\,\hat{\mathbf{p}}\,|u_{n',\boldsymbol{k}}\rangle \times \langle u_{n',\boldsymbol{k}}|\,\hat{\mathbf{p}}\,|u_{n,\boldsymbol{k}}\rangle}{[\varepsilon_n - \varepsilon_{n'}]^2} \tag{4.1}$$

where, $\hat{\mathbf{p}}$ is the momentum operator, $|u_{n,\boldsymbol{k}}\rangle$ is the periodic part of the Bloch function and ε_n is the energy of the n^{th} Bloch band. The summation runs over all the bands including the un-occupied bands. The total Berry curvature is the sum over all the occupied bands, i.e.,

$$\mathbf{\Omega}(\mathbf{k}) = \sum_n f_n \mathbf{\Omega}_n(\mathbf{k}) \tag{4.2}$$

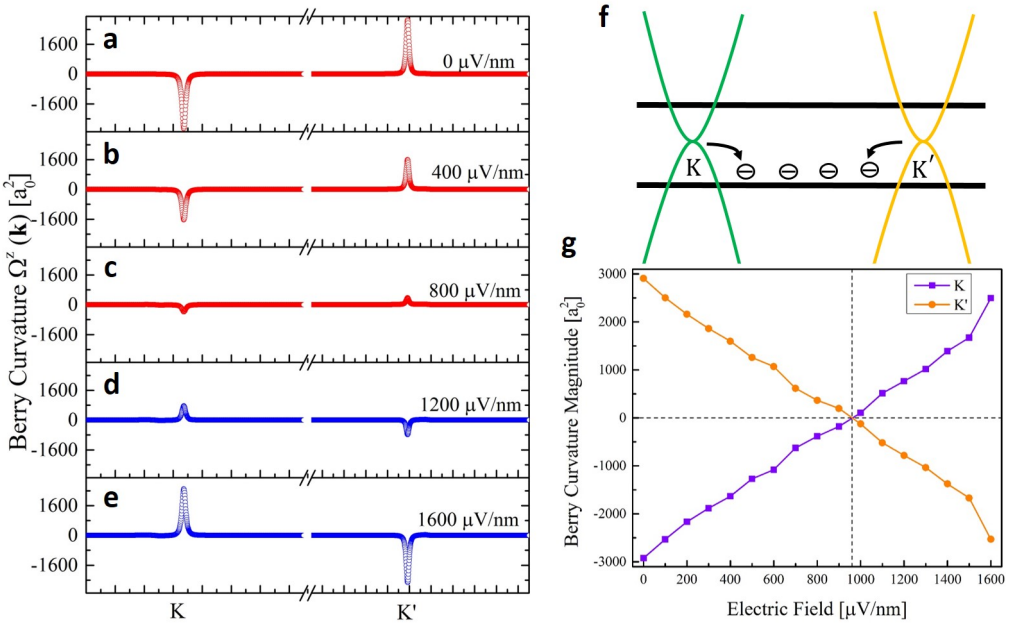

FIGURE 4.2: **a**, A non-zero Berry curvature was observed for ungated bilayer graphene indicating the presence an inherent charge asymmetry persistent in bilayer graphene. This asymmetry comes from the charge transfer to one of the two layers due to electron-electron interaction in neutral bilayer graphene as reported by previous studies (Ref. [34–36]). **b-c** The magnitude of the Berry curvature at both K and K′ high symmetry points decreases with an increase in electric field strength implying the reduction in charge asymmetry as a result of the applied field. **d-e** The polarity of the Berry curvature switches sign after a threshold electric (E$_T$) field and shows an increase in magnitude with an increase in electric field strength. This suggests that the charge asymmetry switches sign at E$_T$; also, the asymmetry grows with the increase in the electric field beyond the threshold electric field. **f** Schematic representation of the charge asymmetry in bilayer graphene, which arises from the charge transfer from valleys to one of the layers (here the electrons are shown to be transferred to the bottom layer). **g** Magnitude of the Berry curvature at both K and K′ valleys at different out-of-plane electric fields. The Berry curvature polarity changes at the threshold electric field E$_T$ = 960 μV/nm.

where f_n is the Fermi-Dirac distribution. Fig. 4.2a-e shows the Berry curvature calculated at different positive electric fields for bilayer graphene. A non-zero Berry curvature is observed at zero electric field (Fig. 4.2a), which is an indication of the asymmetry persistent in pristine bilayer graphene. This observation substantiates the previous reports on asymmetry in bilayer graphene [34–36], which arises from the charge transfer from valleys to one of the layers due to electron-electron interaction, resulting in an interlayer charge asymmetry (Fig. 4.2f). In order to understand the evolution of the asymmetry as well as the Berry curvature, a small out-of-plane electric field, of the order of few hundred μV/nm, is applied in the positive direction. A decrease in the magnitude of the Berry curvature with the increase in the applied external electric field was observed, indicating that the asymmetry is decreasing with the external electric field as it induces charges on the other layer (Fig. 4.2a-c). At a threshold electric field (E_T), 960 μV/nm in this case (Fig. 4.2g), the Berry curvature vanishes which denotes that the charge asymmetry is nullified at this electric field. Increasing the magnitude of the external electric field beyond the threshold electric field results in the change in the direction of the Berry curvature polarity at both the K and K′ high symmetry points.

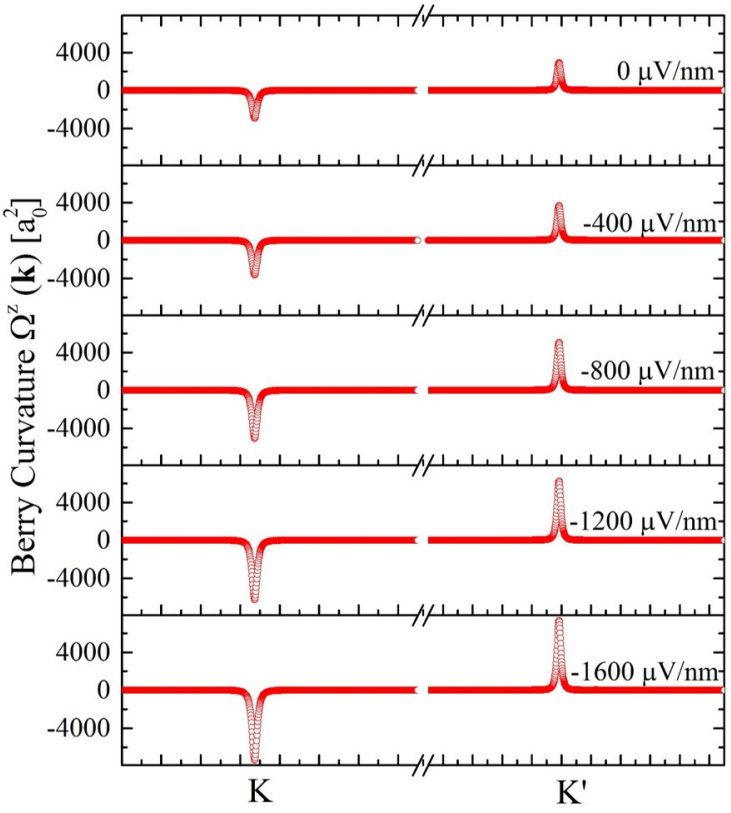

FIGURE 4.3: **a-e** Berry curvature plot for bilayer graphene at different negative electric fields. The Berry curvature at both K and K′ high symmetry points does not show any sign change with the increase in electric field. The increase in the magnitude of the Berry curvature is the result of growing asymmetry in the system with the increase in electric field strength.

Also, once the polarity of the Berry curvature changes, the magnitude of the Berry curvature increases with the increase in the electric field (Fig. 4.2d-e). This implies that the charge asymmetry shifts to the opposite layer beyond the threshold electric field E_T and the asymmetry grows with the further increase in the magnitude of the electric field.

To gain further insight into the development of the asymmetry with the electric field, we performed the Berry curvature calculations at different negative electric fields (Fig. 4.3). The magnitude of the Berry curvature keeps on increasing with the increase in the magnitude of the applied negative electric field. This indicates that negative electric field simply amplifies the inter-layer charge asymmetry persistent in neutral bilayer graphene. This observation also supports the notion of the inherent asymmetry present in ungated bilayer graphene due to long-range Coulomb interaction.

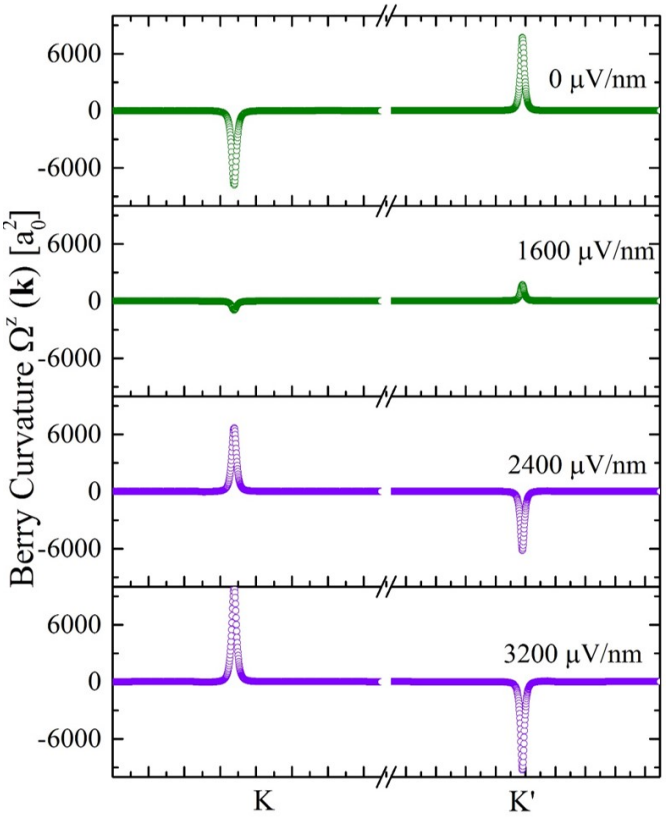

FIGURE 4.4: Berry curvature calculated at different positive electric fields using QUANTUM ESPRESSO (see Methods). **a** As observed in the calculations performed using SIESTA (Fig. 2a, main text), a non-zero Berry curvature with opposite values at K and K′ valleys is observed, validating the argumentation of inbuilt layer asymmetry persistent in neutral bilayer graphene as a result of charge transfer. **b** The increase in electric field reduces the magnitude of the Berry curvature and hence the layer asymmetry. **c** Further increase in the magnitude of the electric field reverses the polarity of the Berry curvature at both K and K′ valleys. This implies that the layer asymmetry shifts to the opposite layer beyond a threshold electric field. **d** Increasing the electric field strength beyond the threshold electric field increases the magnitude of the Berry curvature as a consequence of the increase in layer asymmetry.

All the above calculations are performed using SIESTA code which employs Linear Combination of Atomic Orbitals (LCAO) basis. For a rigorous validation of the results, we performed the same calculations using QUANTUM ESPRESSO which uses plane wave basis (Fig. 4.4). The results mimicked that of SIESTA apart from a slight change in the magnitude of the electric field at which the polarity of the Berry curvature changes. Similar results observed with two different methods (SIESTA and QUANTUM ESPRESSO) which use completely different basis sets manifests the reliability of the results.

4.3 Non-zero band gap in pristine bilayer graphene

As mentioned earlier, the studies predict the existence of an inbuilt asymmetry in bilayer graphene at zero electric and magnetic fields due to charge transfer to one of the layers as a result of electron-electron interaction [34–36]. An internal electric field builds

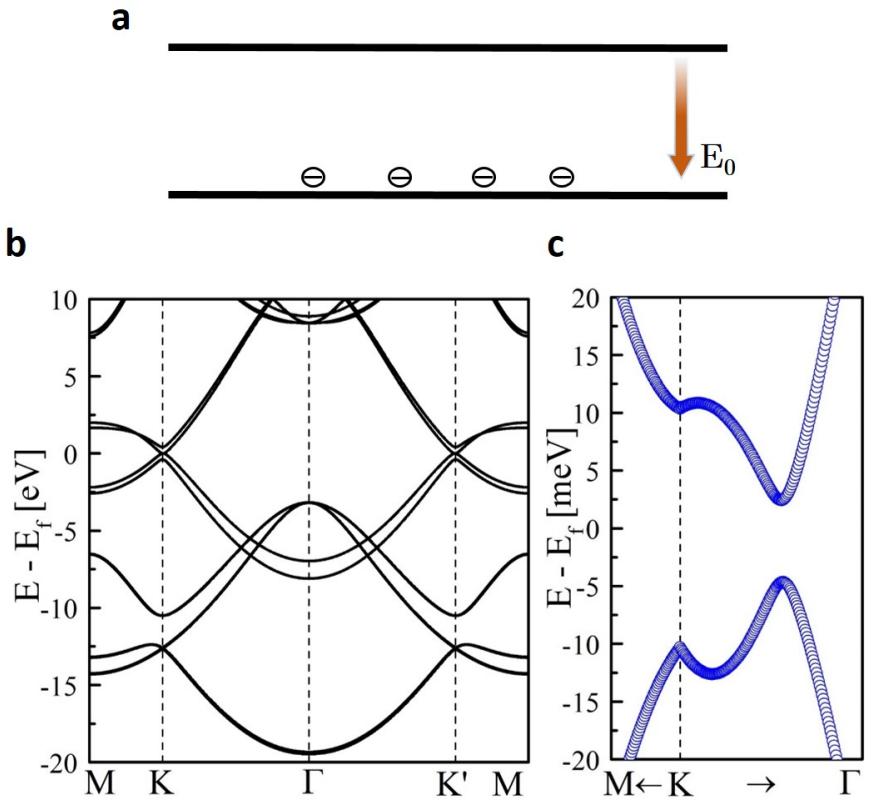

FIGURE 4.5: **a** Schematic representation of the internal electric field developed between the layers in ungated bilayer graphene as a result of layer asymmetry due to charge transfer to one of the layers. **b** Electronic band structure of pristine bilayer graphene showing the valleys at K and K′ high symmetry points. **c** Enlarged view of the bands near the Fermi level around K valley. ungated bilayer graphene shows a small band gap of $\sim$ 7 meV which substantiate the argumentation of asymmetry between the layers.

up across the layers as a result of this charge transfer to one of the layers (Fig. 4.5a). This also creates a potential difference between the layers which should open a band gap in pristine bilayer graphene. Thus, we plotted the band structure of bilayer graphene at zero electric field (Fig. 4.5b). Fig. 4.5c shows the enlarged view of the bands near the Fermi level around K valley. A small band gap of ~ 7 meV was observed in pristine bilayer graphene, which is agreement with the band gap calculated by J. Jung *et al.* using lattice Hartree-Fock approximation [36]. Thus, the observed non-zero band gap also upholds the finding that the non-zero Berry curvature observed is indeed due to the asymmetry present in bilayer graphene due to charge transfer to one of the layers as a result of the electron-electron interaction.

4.4 Berry curvature at high electric fields

We have also calculated the Berry curvature at higher (positive) electric fields i.e., four orders of magnitude higher than the electric field at which Berry curvature switching was observed. The magnitude of the applied electric field is consistent with the experimentally reported values[37]. Fig. 4.6a-c shows the Berry curvature calculated

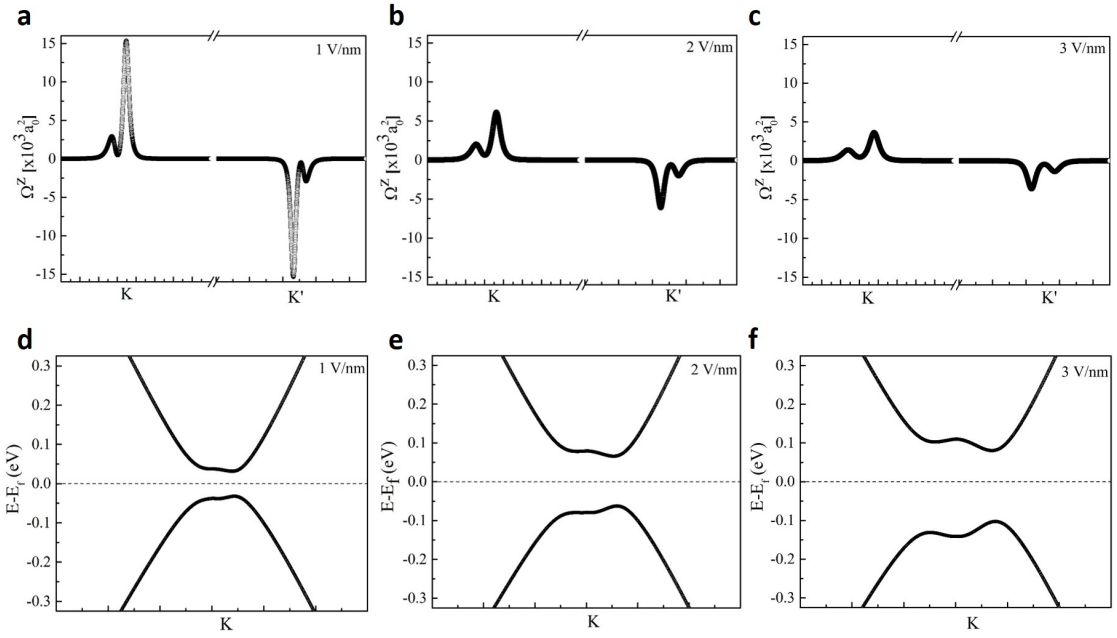

FIGURE 4.6: Berry curvature calculated at K and K′ high symmetry points **a** for 1 V/nm **b** for 2 V/nm and **c** for 3 V/nm. The magnitude of the Berry curvature decreases with the increase in the electric field at higher electric fields, in contrast to what is observed at lower electric fields (Fig. 4.2d,e). This is due to the large band gap opening at higher electric fields because Berry curvature is inversely proportional to the square of the energy difference between conduction band minimum and valence band maximum. **d-f** Enlarged view of the bands near the Fermi level around K valley **d** for 1 V/nm **e** for 2 V/nm and **f** for 3 V/nm.

at the electric fields 1 V/nm, 2 V/nm and 3 V/nm respectively. The magnitude of the Berry curvature rapidly decreases as the magnitude of the electric field increases at higher electric fields. This is in contrast to what was observed at lower electric fields, once the Berry curvature polarity is switched. Also, the delocalization of the Berry curvature in the momentum space increases with the increase in the electric field at higher fields. This has also been shown by plotting the Berry curvature in the 2D k-space(Fig. 4.7). The above findings can be explained by analyzing the expression for Berry curvature(Eq. (1.1)). Taking the derivative of the periodic part of the Bloch function (Eq. (1.1)) makes the calculation cumbersome. As per Wannier interpolation scheme, the Berry curvature, calculated in terms of the Wannier functions [21] using finite differences is defined as,

$$\mathbf{\Omega}(\mathbf{k}) = \sum_{n} f_n \overline{\mathbf{\Omega}}^{H}_{nn} + \sum_{n,m} (f_m - f_n) \mathbf{D}^{H}_{nm} \times \overline{\mathbf{A}}^{H}_{nm} + \mathbf{\Omega}^{DD} \tag{4.3}$$

where $\overline{O}^{H} = U^{\dagger} O^{W} U$ represent the components which transform covariently from Wannier gauge (W) to Hamiltonian gauge (H) under unitary transformation U ; and

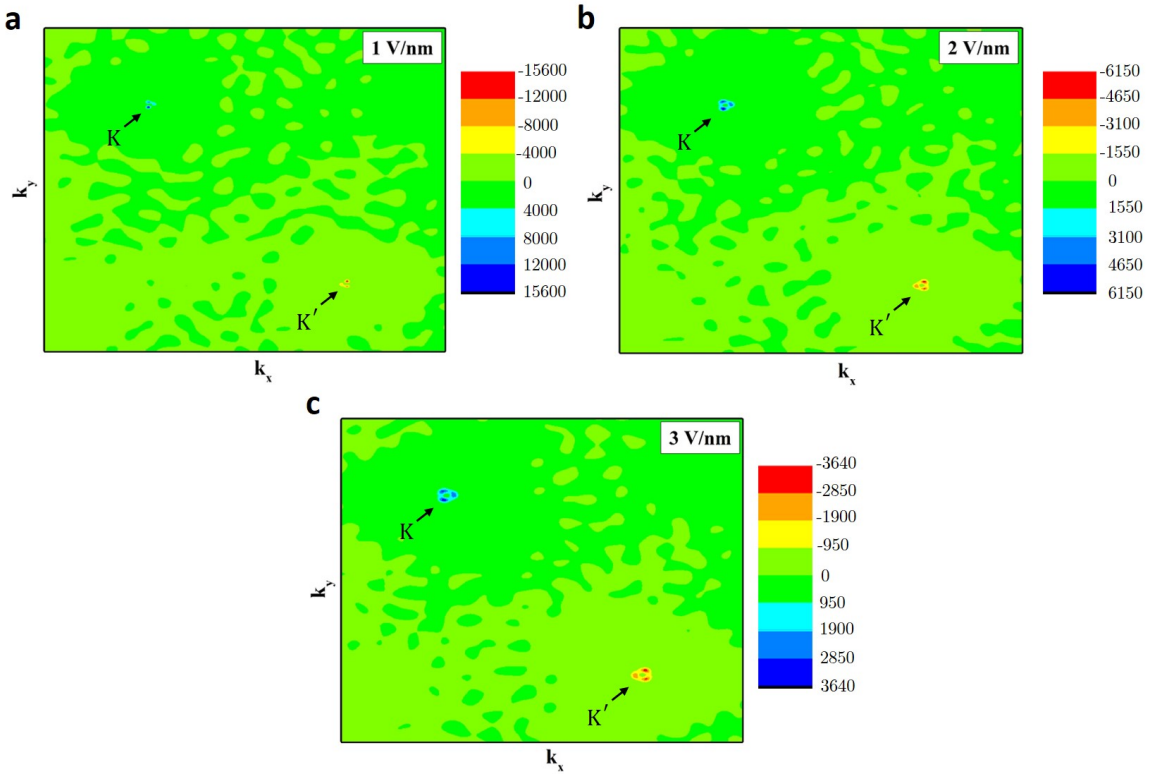

FIGURE 4.7: Berry curvature plotted in the 2D k-space **a** for 1 V/nm, **b** for 2 V/nm, and **c** for 3 V/nm. At higher electric fields, the Berry curvature delocalizes and spreads across the 2D k-space with the increase in the strength of the applied out-of-plane electric field.

$\boldsymbol{D}^H_{nm} = \frac{(U^\dagger \nabla H^W U)_{nm}}{\varepsilon_m - \varepsilon_n}(1 - \delta_{nm})$. The last term is defined as

$$\boldsymbol{\Omega}^{DD} = \frac{i}{2}\sum_{n,m}(f_n - f_m)\frac{(U^\dagger \nabla H^W U)_{nm} \times (U^\dagger \nabla H^W U)_{nm}}{(\varepsilon_m - \varepsilon_n)^2} \tag{4.4}$$

Here, H^W is the Hamiltonian in Wannier representation and ε_n is the energy of the n^{th} band.

The summation runs over all the Wannier states, which is, all the occupied and two un-occupied states in our case. The term $(f_n - f_m)$ in Eq. (4.4) tells that a pair of occupied states or un-occupied states have negligible contribution to the total Berry curvature. Thus, a pair of bands, one of them occupied and another one un-occupied contribute extensively to the total Berry curvature. In that case, ε_m and ε_n are the energies of these occupied and un-occupied valleys respectively. Hence increasing the band gap results in the decrease in total Berry curvature because Berry curvature is inversely proportional to the square of the energy difference between conduction band minimum and valence band maximum. In the case of bilayer graphene, the band gap increases with the increase in the strength of the applied electric field (Fig. 4.6d-f). The band gaps are measured to be 64 meV, 126 meV and 183 meV for 1 V/nm, 2 V/nm and 3 V/nm respectively. Thus, as the Berry curvature is proportional to the inverse of the square of the band gap, its magnitude decreases with the increasing field strength. This findings elucidates the fact that the application of very high electric field is not desirable in bilayer graphene valleytronic devices. Also, the delocalization of the Berry curvature in the k-space at high electric fields may increase the intervalley scattering which is undesirable for a valleytronic material. The splitting of the Berry curvature arises from the formation of the Mexican hat in the band structure of bilayer graphene near the valleys at higher electric fields.

4.5 Berry curvature in AA-stacked bilayer graphene

Bilayer graphene exhibits another stacking configuration apart from the usually studied AB-stacking which is AA-stacking. It, therefore, becomes inevitable to investigate the valleytronics properties of AA-stacked bilayer graphene. Thus, we have carried out the Berry curvature calculations for AA-stacked bilayer graphene. Fig. 4.8 shows the Berry curvature calculated near high symmetry points K and K′ for AA-stacked bilayer graphene. No Berry curvature was observed at zero electric field indicating the symmetry persistent in the system (Fig. 4.8a). In order to examine if applying an out-of-plane electric field can break the symmetry and show any valleytronic property, a large electric field (1 V/nm, 2 V/nm, and 3 V/nm) was applied (Fig. 4.8b-d).

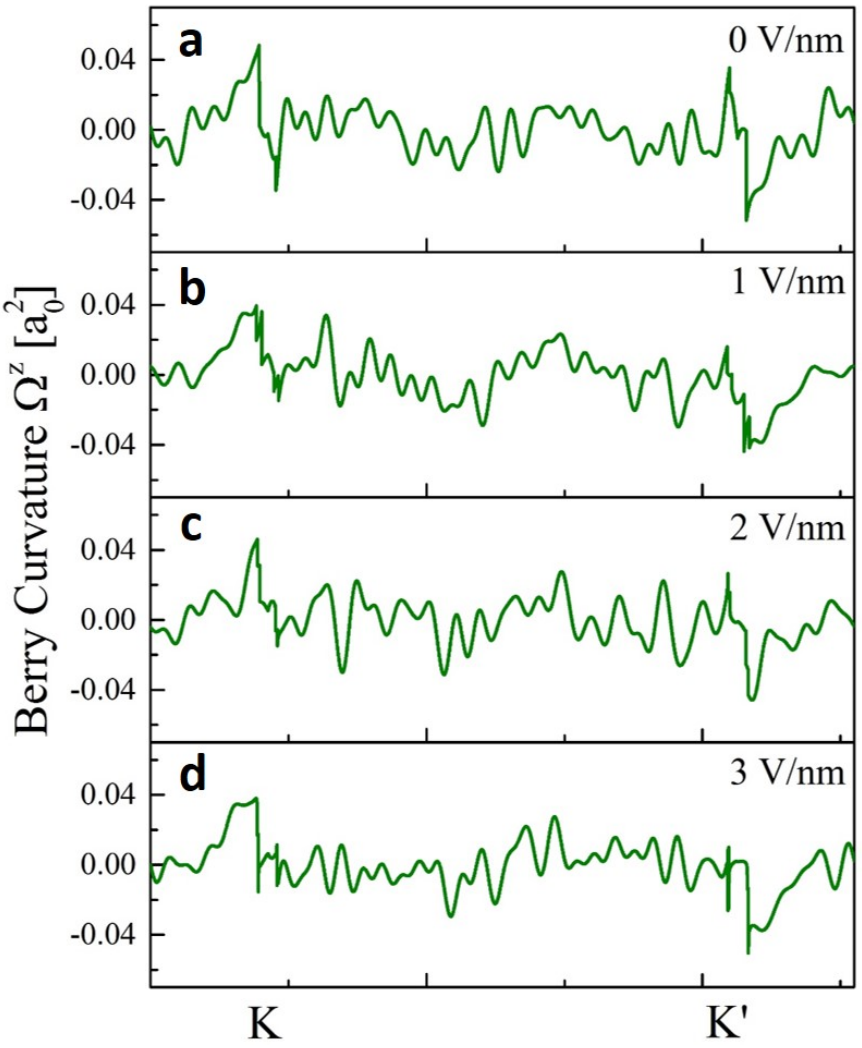

FIGURE 4.8: **a** No berry curvature was observed in ungated AA-stacked bilayer graphene implying that the system is symmetric. Berry curvature calculated at out-of-plane electric fields **b** 1 V/nm **c** 2 V/nm and **c** 3 V/nm. The absence of Berry curvature in the presence of an out-of-plane electric field which induce interlayer potential difference implies that the symmetry of the system remains uninfluenced by the field.

However, no Berry curvature was observed under the application of out-of-plane electric field as well. This signifies that an interlayer potential difference does not break the layer symmetry in AA-stacked bilayer graphene. To validate these findings, we plotted the band structure of AA-stacked bilayer graphene at different out-of-plane electric fields near the Fermi level, around the K point (Fig. 4.9a-d). As anticipated from the above findings, no band gap opening was observed under the application of an out-of-plane electric field. This implies that AA-stacked bilayer graphene remains layer symmetric under an interlayer potential difference and does not show any valleytronic properties such as Berry curvature.

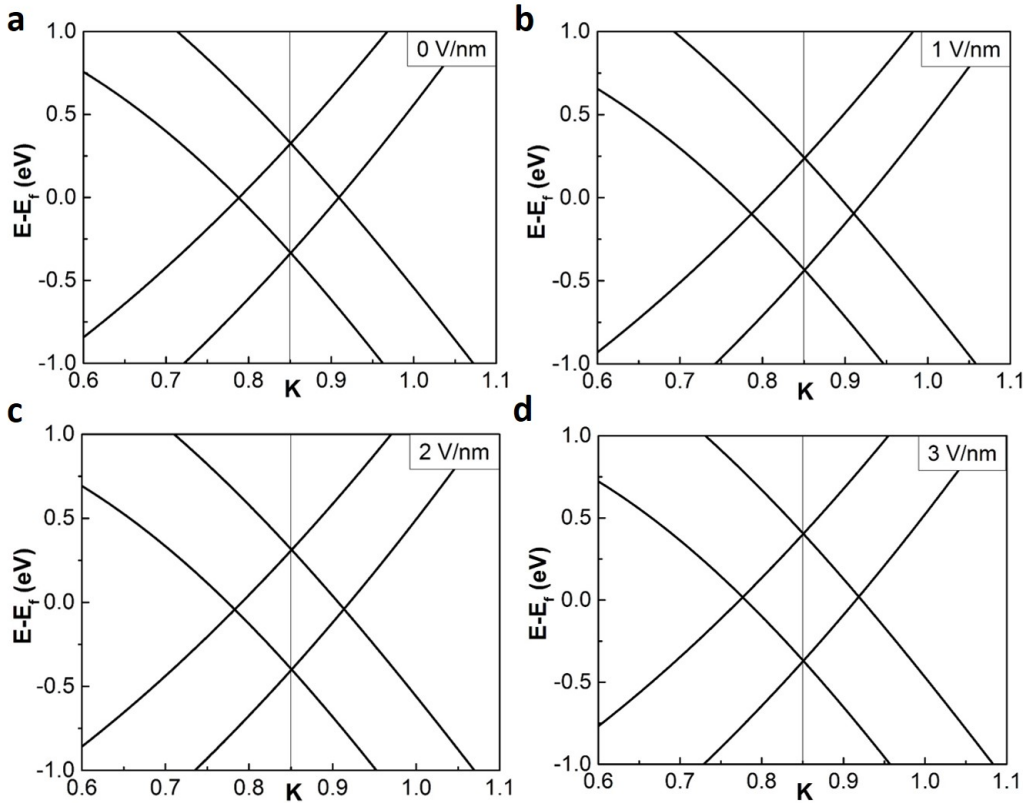

FIGURE 4.9: **a** No berry curvature was observed in ungated AA-stacked bilayer graphene implying that the system is symmetric. Berry curvature calculated at out-of-plane electric fields **b** 1 V/nm **c** 2 V/nm and **c** 3 V/nm. The absence of Berry curvature in the presence of an out-of-plane electric field which induce interlayer potential difference implies that the symmetry of the system remains uninfluenced by the field.

4.6 Bilayer graphene valley valve

Our findings can also pave the way to a novel type of valley valve. Several proposals are made so far to construct valley filter and valley valve in graphene-based devices. But they either demand highly complicated fabrication such as perfect zigzag edges [44, 45] or dual gate splitting with opposite potential at both the gates [46]. In contrast, we propose a valley valve which can be operated with a single gate at the center of the bilayer graphene ribbon. Also, this scheme does not rely on any complicated device fabrication.

A valley valve allows the current to pass through when Berry curvature at K (or K′) valleys have the same polarity throughout the direction of motion of the carrier; on the other hand, if the polarity of the Berry curvature is opposite at any portion in the direction of motion of the carriers, the current is blocked. Fig. 4.10 shows the schematic representation of the working principle of a valley valve with a single gate at the center of the graphene nanoribbon. The operation of the valve depends on the magnitude of the

out-of-plane electric field applied by the gate at the center. Because the polarity of the Berry curvature depends on whether the applied electric field is greater than or less than the threshold electric field (E_T). If an electric field greater than the threshold electric field, E_T is applied, the system blocks the valley current since the region between the two gates have opposite polarity for Berry curvature with respect to either side of the device (Fig. 4.10a). Conversely, an electric field, which is less than the threshold electric field, E_T allows the valley current to pass through as the direction of Berry curvature is same on the entire length of the device (Fig. 4.10b).

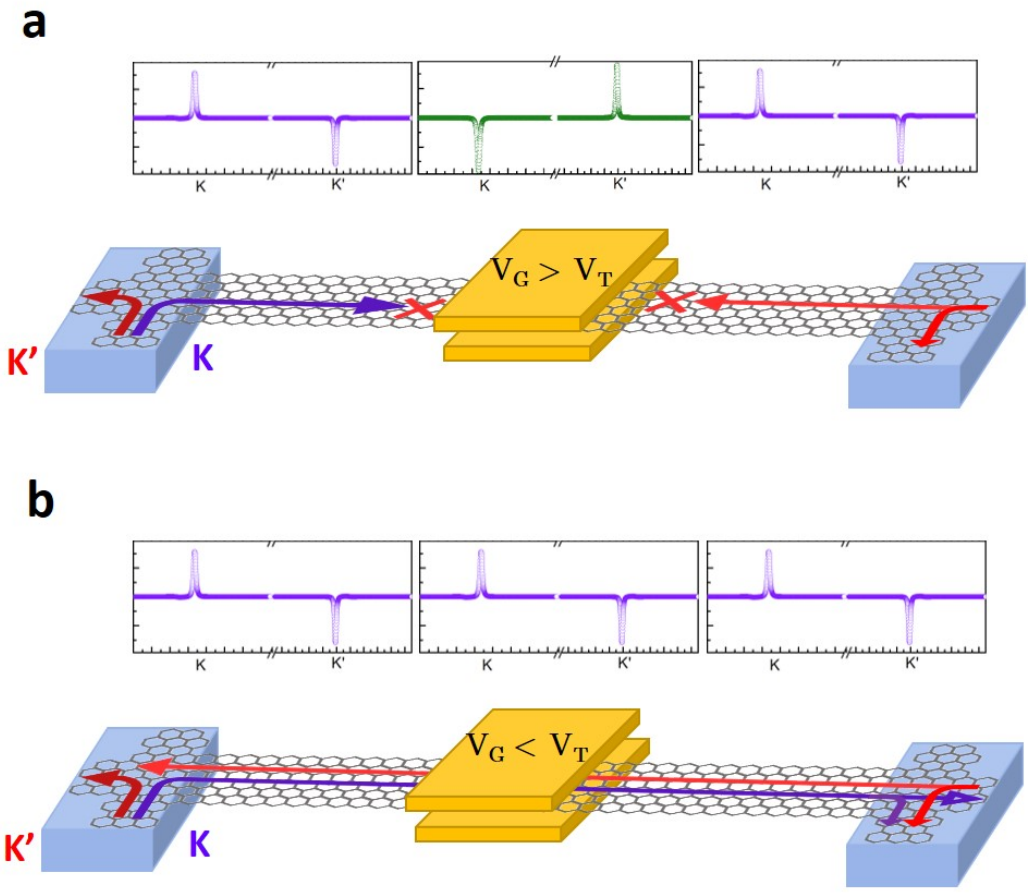

FIGURE 4.10: In a valley valve, the carriers from the K (or K′) valleys pass through when the polarity of the Berry curvature is the same throughout the direction of motion of the carriers; for opposite polarities, the current is blocked. **a** When a gate voltage greater than V_T (V_T is the gate voltage corresponding to the threshold electric field E_T) is applied at the central gate, the Berry curvature polarity at the region of bilayer graphene between the gates becomes opposite to that of the ungated region at either sides of the gate (top panel). This stops the carriers from either valley to pass through. **b** On the other hand, if the gate voltage is less than V_T, all the regions including the region between the gates have same polarity for the Berry curvature (top panel). This allows the carriers to pass the gate to the other end of the device.

4.7 Summary

In conclusion, we validate the presence of an asymmetry in ungated, undoped bilayer graphene with the observation of a non-zero Berry curvature. The polarity of the Berry curvature changes with the sign of layer polarization. The nonobservation of the valley current induced by Berry curvature at zero electric field in previous experimental studies on bilayer graphene (ref. [42], ref. [43]) could be due to the following reasons; (i) the high temperature at which the experiment was performed (70 K); carriers can overcome the energy gap due to thermal excitation, (ii) the cleanliness of the sample; gapped states are expected to be present only in the highest quality samples [39, 40] and (iii) the screening of the Coulomb interaction by the substrate; in both the studies, bilayer graphene was encapsulated by h-BN layers, which can suppress the electron-electron interaction [47]. In addition, the asymmetry present in ungated bilayer graphene is vulnerable to slight changes in charge density, out-of-plane electric field, and disorder [40]. Thus a dedicated and systematic experimental study is necessary to observe Berry curvature and hence valley current in ungated bilayer graphene.

Chapter 5

Manipulating Berry curvature in hBN-Bilayer graphene heterostructure

Berry curvature, which arises from the asymmetry in a system is a paramount physical property which results in interesting phenomenon such as valley hall effect. There have been several experimental observations of valley hall effect in hBN encapsulated bilayer graphene systems and hBN-single layer graphene heterostructures. Although the role of hBN in breaking the layer symmetry in bilayer graphene and sublattice symmetry in single layer graphene is well known, the effect of the alignment and orientation of hBN layer on the emergence of Berry curvature in these systems is not studied in detail yet. We show that the arrangement of the hBN layer has a significant effect on the Berry curvature of the bilayer graphene system, which can further be manipulated by applying a perpendicular electric field. However, single layer graphene hBN systems are rather insensitive to the configuration of the hBN layer as well as to the application of the electric field.

5.1 Introduction

Introduction of two-dimensional materials have led to the observation of several interesting physical phenomena experimentally [14, 15], including Berry phase which is a geometrical phase theoretically predicted a few decades back [1]. Berry phase was experimentally observed and measured to be π and 2π in single layer graphene and bilayer graphene respectively [54, 55]. Observation of this geometrical phase has also lead to the quest for physical phenomenon associated with it such as Berry curvature

and orbital magnetic moment[3, 4]. Berry curvature, which arises as a consequence of inversion symmetry breaking, can be considered as a pseudo-magnetic field in the reciprocal lattice. It serves as the driving force for carriers in valley Hall effect (VHE), where the electrons from K and K′ valleys of the hexagonal lattice move to opposite edges of the material in the presence of an in-plane electric field[27, 56]. VHE and associated valley current are observed in graphene-based devices through non-local electrical measurement [42, 43, 57]. In these devices, hexagonal boron nitride (hBN) layer is used as a substrate which can break the sublattice symmetry in single layer graphene (SLG), or as a dielectric encapsulation layer. However, a detailed analysis on the role of the hBN layer and its orientation in inducing Berry curvature in a single layer and bilayer graphene (BLG) is still lacking. Thus herein we study the emergence of Berry curvature and its manipulation in hBN-BLG and hBN-SLG heterostructures.

The *ab initio* calculations. calculations are performed within density-functional theory using the Linear Combination of Atomic Orbitals (LCAO) method implemented in the package SIESTA [48]. van der Waals exchange correlation functionals [49] were used in order to obtain the interlayer distance in close proximity to the experimental values. A vacuum layer of thickness 20 Åwas used to avoid the interaction between adjacent bilayers. A fine Monkhorst-Pack grid of 36 x 36 x 1 and a mesh cut off of 400 Ry was used in all the calculations. The atomic positions are optimized until the force on each atom is less than 0.01 eV/Å. The electronic charge density is calculated using Denchar package included in SIESTA. The Berry curvature calculations are performed using the Wannier90 package which follows the Wannierization procedure [50]. A total of ten Wannier functions are constructed on a fine Monkhorst-Pack grid of dimension 36 x 36 x 1. In the disentanglement procedure, the Wannier spread is converged down to 10^{-10} Å^2 in less than 600 iterations.

Berry curvature for the nth band is defined as

$$\mathbf{\Omega}_n(\mathbf{k}) = i\frac{\hbar^2}{m^2}\sum_{n\neq n'}\frac{\langle u_{n,\boldsymbol{k}}|\,\hat{\mathbf{p}}\,|u_{n',\boldsymbol{k}}\rangle \times \langle u_{n',\boldsymbol{k}}|\,\hat{\mathbf{p}}\,|u_{n,\boldsymbol{k}}\rangle}{[\varepsilon_n - \varepsilon_{n'}]^2} \tag{5.1}$$

where, $\hat{\mathbf{p}}$ is the momentum operator, $|u_{n,\boldsymbol{k}}\rangle$ is the periodic part of the Bloch function and ε_n is the energy of the n^{th} Bloch band. The total Berry curvature is the sum over all the occupied bands, i.e.,

$$\mathbf{\Omega}(\mathbf{k}) = \sum_n f_n \mathbf{\Omega}_n(\mathbf{k}) \tag{5.2}$$

As per the Wannier interpolation scheme [**?**], a pair of occupied states or a pair of un-occupied states have a negligible contribution to the total Berry curvature. Thus, a pair of bands, one of them occupied and another one un-occupied contribute extensively to the Berry curvature. This was previously observed in the case of the avoided crossing

where an external perturbation can control the gap between the two bands [58**?** , 59]. The small energy difference between the bands in avoided crossing substantially increases the Berry curvature. In the case of single-layer graphene, such a pair of bands, the bands above and below the Fermi level comes from the A and B sublattices of the unit cell. On the other hand, in bilayer graphene, these low energy bands arise from the non-dimer carbon atoms (the atoms exactly one above the other is called dimer atoms and the other pair are called non-dimer atoms) of the unit cell. Thus altering the potential of these atoms can open up band gap and induce Berry curvature in these systems. This can be achieved by aligning the hBN layer to the graphene in such a way that the nitrogen (N) and the boron (B) atoms of the hBN layer comes above and/or below the non-dimer carbon (C) atoms which contribute to the low energy bands.

5.2 hBN-BLG Heterostructure

The effect of the hBN layer as a substrate is studied using hBN-BLG heterostructure where the BLG is aligned on top of hBN (Fig. 5.1a, inset). The N and B atoms of the hBN layer are placed such a way that they are below B1 and A2 non-dimer atoms of the bilayer graphene respectively. The dimer atoms come at the center of the hexagonal ring of the hBN layer. Fig. 5.1a shows the Berry curvature calculated for the heterostructure along K and K′ high symmetry points of the Brillouin zone. Under zero electric field, the system shows a non-zero Berry curvature with opposite values at the two (K and K′) symmetry points. This implies that the system has broken inversion symmetry which comes from the difference in the potential experienced by the two layers of the bilayer graphene due to the presence of the hBN layer at the bottom. Application of a positive electric field (1 V/nm) across the heterostructure switches the polarity of the Berry curvature at both the high symmetry points, which indicates that the asymmetry between the layers has switched with the application of a positive electric field. we have also studied the band structure of the system around the Fermi level near K (Fig. 5.2b). The presence of hBN has induced a band gap of 36 meV in the ungated hetrostructure. Application of a positive electric field has reduced the band gap (23 meV) which also explains the increase in the magnitude of the Berry curvature with application of the electric field. A narrow gap between one occupied and another un-occupied bands results in a large Berry curvature as mentioned earlier. In order to understand further and to confirm the asymmetry between the layer, we have plotted the difference in charge density between the layers (DCDBL) i.e. the charge density of the second layer subtracted from the first layer of the bilayer graphene. Fig. 5.1c shows the DCDBL of the system at zero electric field. Positive value demonstrates the regions where the bottom layer has more charges than the top layer, whereas, the negative value

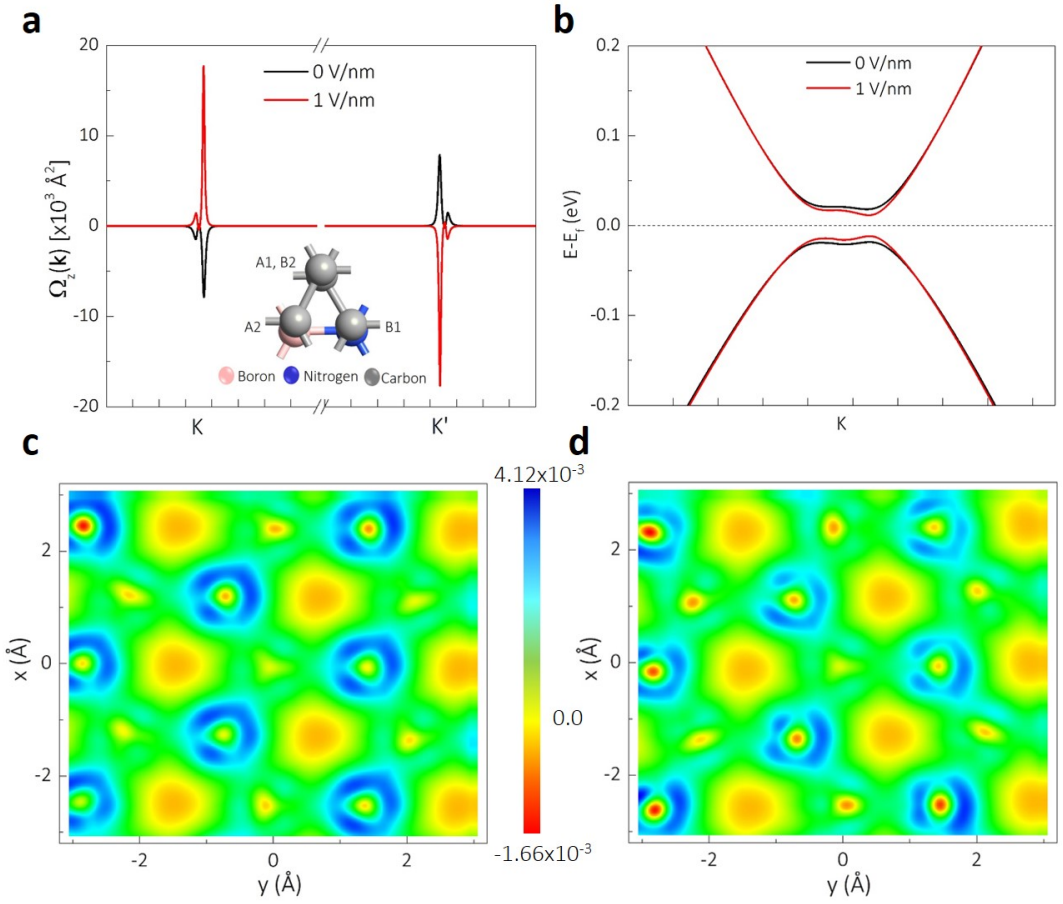

FIGURE 5.1: **a** Berry curvature calculated for the hBN-BLG heterostructure (shown in the of inset figure a) along the K and K′ high symmetry points of the Brillouin zone for 0 V/nm and 1 V/nm. **b** Band structure of the hetrostructure around the Fermi level near K for 0 V/nm and 1 V/nm. **c** Difference in charge density between the layers (DCDBL) i.e. the charge density of the second layer subtracted from the first layer of the bilayer graphene at 0 V/nm. **d** DCDBL for the system at 1 V/nm.

indicates the regions where the top layer has more charges than the bottom layer. The non-zero difference in the charge density indicates the asymmetry between the layers which in turn results in the emergence of the Berry curvature. However, application of a positive electric field (1 V/nm) induces charges on the top layer, reducing the positive DCDBL in the heterostructure (Fig. 5.1d). This reverses the polarity of the layer asymmetry and hence the Berry curvature.

5.3 hBN-BLG-hBN Heterostructure

5.3.1 NCB/BCN Configuration

We have also studied encapsulated bilayer graphene where bilayer graphene is sandwiched between hBN layers (Fig. 5.2a, inset). The hBN layers are arranged such

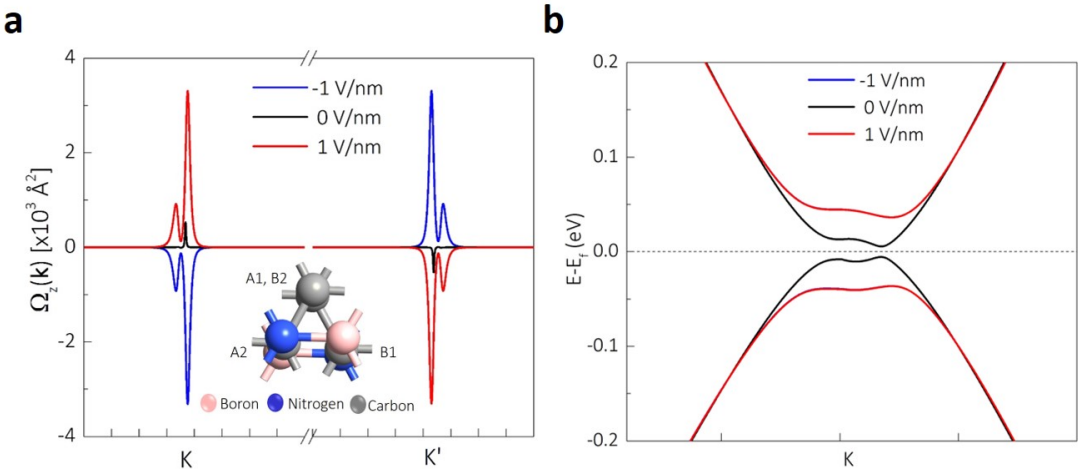

FIGURE 5.2: **a** Berry curvature calculated for the hBN-BLG-hBN heterostructure (for NCB/BCN configuration shown in the of inset figure a) K and K′ high symmetry points of the Brillouin zone for 0 V/nm, 1 V/nm and -1 V/nm. **b** Band structure of the hetrostructure around the Fermi level near K for 0 V/nm, 1 V/nm and -1 V/nm.

that the top hBN is opposite to that of the bottom one. At B1 site, N and B atoms are at the bottom and top respectively, whereas, at A2, B is at the bottom and N is at the top (NCB/BCN). Fig. 5.2a shows the Berry curvature calculated along the K and K′ points of the Brillouin zone for 0 V/nm, 1 V/nm and -1 V/nm. For the ungated case (0 V/nm), the heterostructure shows a small Berry curvature which is very much confined to the k-space. This arises from the asymmetry in the bilayer graphene due to the spontaneous charge transfer from the valleys to one of the layers, which will be discussed elsewhere [60]. This also shows that encapsulation of bilayer graphene with hBN layers does not make any difference to the basic properties of bilayer graphene apart from providing additional screening. Thus, encapsulated bilayer graphene is the better alternative to observe valley Hall effect in ungated bilayer graphene as the asymmetry in free-standing graphene is vulnerable to the potential difference, charge imbalance and disorder [39, 40]. However, application of out-of-plane electric field results in a fairly large magnitude of the Berry curvature and the Berry curvature is widely spread over the k-space compared to the ungated case. The Berry curvature polarity is also tunable with the direction of the electric field. Fig. 5.2b shows the band structure for the system around the Fermi level at K. The small band gap opening in the ungated case comes from the spontaneous chargre transfer discussed above. Applying a perpendicular electric field opens a large band gap (73 meV) which has equal magnitude for both positive and negative electric fields. This is due to the large asymmetry between the layers induced by the electric field. In order to understand the origin of the Berry curvature we plotted the DCDBL for the system at -1 V/nm, 0 V/nm and 1 V/nm (Fig. 5.3a-c). Although the DCDBL is not apparent as it was in the case of hBN-BLG due to the near symmetry of the system, a close inspection reveals that the application of positive and negative electric

fields induces charges in the top and bottom layers respectively. Thus, the polarity of the layer asymmetry and hence that of the Berry curvature changes with the direction of the electric field.

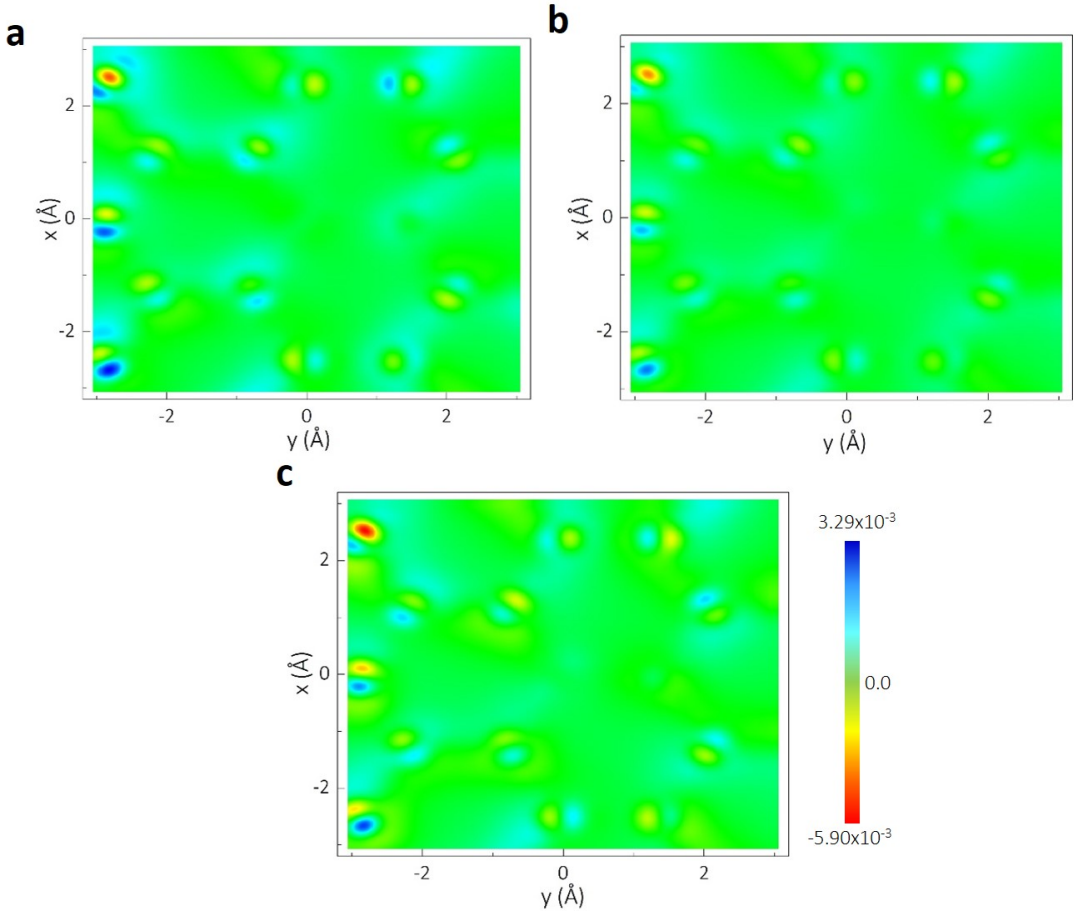

FIGURE 5.3: DCDBL of hBN-BLG-hBN system with NCB/BCN configuration for **a** -1 V/nm **b** 0 V/nm and **c** 1 V/nm.

5.3.2 NCN/BCB Configuration

In order to find the effect of the alignment of the hBN layer on the layer symmetry of the encapsulated bilayer graphene, we inverted the top hBN layer (Fig. 5.4a, inset). In this configuration, the B and N atoms on the top and bottom hBN layers are one above the other. More specifically, the B1 non-dimer atom has nitrogen at the top and bottom, whereas, A2 non-dimer atom has boron atoms at the top and bottom (NCN/BCB). Fig. 5.4a shows the Berry curvature calculated along the high symmetry points of the Brillouin zone for this heterostructure. The heterostructure shows a non-zero Berry curvature which is spread over the k-space. This implies that the orientation of the hBN layer also has a significant role in breaking the symmetry between the layers of the bilayer graphene. Also, this asymmetry can be reversed with

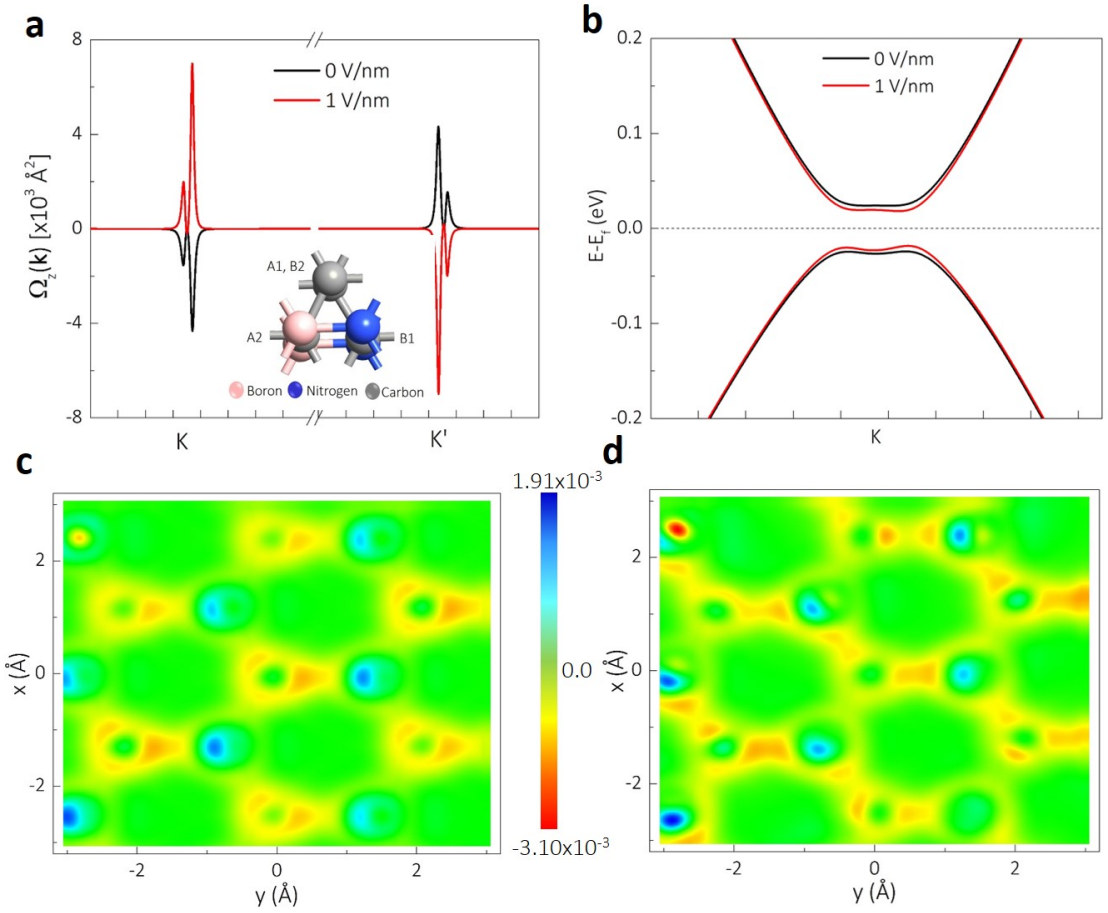

FIGURE 5.4: **a** Berry curvature calculated for the hBN-BLG-hBN heterostructure (for NCN/BCB configuration shown in the of inset figure a) along the K and K′ high symmetry points of the Brillouin zone for 0 V/nm and 1 V/nm. **b** Band structure of the hetrostructure around the Fermi level near K for 0 V/nm and 1 V/nm. DCDBL for the system is plotted at **c** 0 V/nm and **d** 1 V/nm.

the application of a positive electric field across the layers, which can be seen from the reversal of the Berry curvature polarity at 1 V/nm. The band structure studies shows that inverting the orientation of the top hBN layer results in the openign of the band gap (48 meV) in the heterostructure. However, application of a positive electrid field reduces the band gap to 37 meV. This also explains the increase in the magnitude of the Berry curvature at 1 V/nm as indicated in the case of hBN-BLG system. The DCDBL carried out for the ungated case (Fig. 5.4c) shows non zero values indicating that the two layers of the bilayer graphene experience difference potential in this configuration. This induces charge asymmetry between the layers and hence a non-zero Berry curvature. Application of a positive electric field across the layers changes the DCDBL (Fig. 5.4d) and reverses the polarity of the layer asymmetry which further reverses the polarity of the Berry curvature.

5.4 hBN-SLG and hBN-SLG-hBN Heterostructures

For completion, hBN-single layer graphene heterostructures with and without encapsulation are also studied. In contrast to the breaking of layer symmetry in bilayer graphene, the A/B sublattice symmetry is broken in single layer graphene due to the presence of hBN layer. Fig. 5.5a shows the unit cell of the single layer graphene on hBN heterostructure with one carbon atom above the nitrogen atom and the other carbon atom at the center of the hBN hexagonal ring (hBN-SLG). The Berry curvature calculated along the high symmetry points for the hBN-SLG system is shown in Fig. 5.5d. ungated hBN-SLG shows a non-zero Berry curvature which has opposite values at K and K′ high symmetry points. The asymmetry comes from the unequal potential experienced by the A and B sublattice caron atoms due to the presence of two different atoms (Nitrogen and Boron) in the bottom hBN layer. In order to study the effect of electric field on the polarity as well as the magnitude of the Berry curvature, we applied a positive (1 V/nm) and a negative (-1 V/nm) electric fields across the layers of the heterostructure. However, unlike the bilayer graphene case, application of an out-of-plane electric field does not invert the polarity of the Berry curvature either in the positive or in the negative electric field case for hBN-SLG heterostructure. The magnitude of the Berry curvature slightly varies with the applied electric field. The band

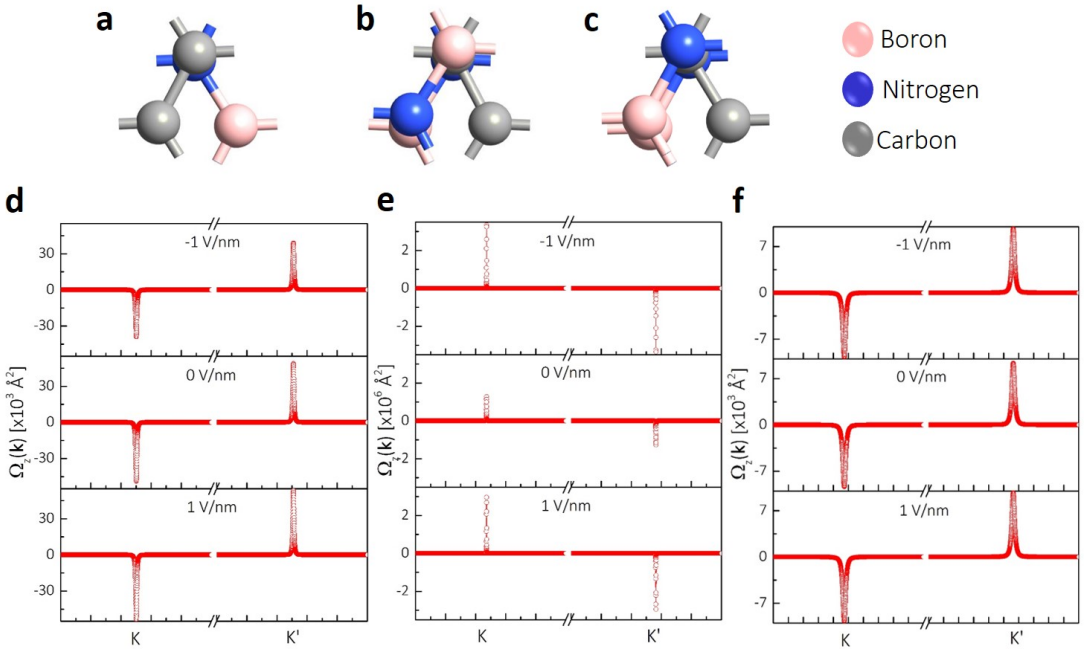

FIGURE 5.5: **a** Unit cell of the single layer graphene hBN heterostructure. Encapsulated graphene-hBN heterostucture with **b** NCB configuration and **c** NCN configuration. Berry curvature calculated at -1 V/nm, 0 V/nm and -1 V/nm for **d** hBN-SLG heterostructure, **e** hBN-SLG-hBN heterostructure with NCB configuration and **f** hBN-SLG-hBN heterostructure with NCN configuration.

structure calculated for hBN-SLG system (Fig. 5.6 a) also shows that the application of a perpendicular electric field have only mild effect in modifying the band structure.

For the encapsulated single-layer graphene, two configurations are considered. One in which the top hBN layer is aligned opposite to that of the bottom hBN (NCB) as shown in Fig. 5.5b and another in which the hBN layers on the top and bottom are aligned in phase with each other (NCN) as shown in Fig. 5.5c. In NCB configuration, one C atom has N at the bottom and B at the top, while the other C atom comes at the center of the hBN hexagonal ring. Fig. 5.5e shows the Berry curvature calculated along the K and K′ points of the Brillouin zone for NCB arrangement. A non-zero Berry curvature which is highly constrained to the k-space in comparison to the hBN-SLG case is observed. Also, the magnitude of the Berry curvature is larger than the hBN-SLG case by at least two orders. A perpendicular electric field of magnitude 1 V/nm is applied across the layers in both the directions. It is found that application of perpendicular electric field does not have any effect on the polarity of the Berry curvature encapsulated case as well. However, an out-of-plane electric field can alter the magnitude

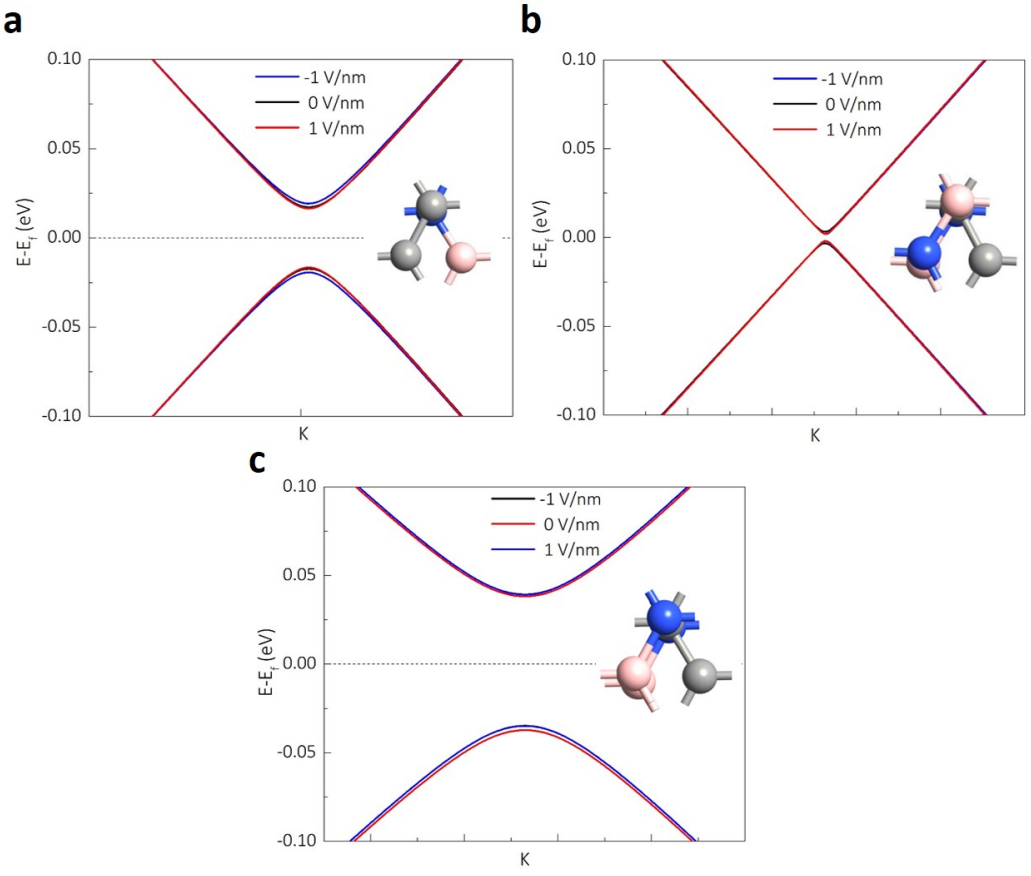

FIGURE 5.6: **a** Band structure calculated for hBN-SLG heterostructure for -1 V/nm, 0 V/nm and 1 V/nm. Band structure calculated for encapsulated single layer graphene at -1 V/nm, 0 V/nm and 1 V/nm **b** with NCB configuration and **c** NCN configuration.

of the Berry curvature. The hihgly constrained Berry curvature is a consequence of the near symmetry of the system. The band structure of the system (Fig. 5.6 b) resembles that of pristine bilayer graphene with sharp diract cones at the K point. Also the applied electric fields does not alter the band structure. In NCN arrangement, one C atom has N atom at the top as well as at the bottom and the other C atom is at the center of the hexagon formed by hBN layers. The Berry curvature calculated at 0 V/nm as well as at 1 V/nm and -1 V/nm (Fig. 5.5f) showcases similar behavior to that of the previous case. A non-zero Berry curvature is observed at zero electric field whose magnitude can be tuned with the electric field. The polarity of the Berry curvature does not change with the application of the electric field. Nonetheless, it can be observed that the Berry curvature is spread more over the k-space in comparison to the other configurations of the single layer graphene. This is also evident from the band structure of the system (Fig. 5.6 c) which is parabolic at the K point unlike the sharp conical shape in the case of NCB configuration. Thus the alignment of the hBN layer does not have any effect in altering the polarity of the Berry curvature.

5.5 Summary

In conclusion, we have studied the emergence of Berry curvature in hBN-bilayer graphene and hBN-single layer graphene systems for various configurations of the hBN layer. The effect of positive as well as negative electric fields is also studied. In the case of bilayer graphene heterostructure, hBN induces layer asymmetry and hence the Berry curvature. The electric field could manipulate the polarity as well as the magnitude of the Berry curvature depending on the direction of the applied field. On the other hand, the polarity of the Berry curvature could not be reversed with the application of an out-of-plane electric field in hBN single-layer graphene systems although the magnitude of the Berry curvature was dependent on the applied electric field.

Chapter 6

Substrate Induced Valley Hall Effect in Bilayer Graphene

Bilayer graphene is widely studied for valleytronics due to its high quality and properties. However, none of the experimental studies conducted so far has observed valley Hall effect induced valley current in ungated bilayer graphene due to the symmetry present in the system. Although there are several studies on the existence of asymmetry in ultraclean ungated bilayer graphene, it is very challenging to realize. However, in this study, we have observed a non-zero valley current induced by Berry curvature in ungated bilayer graphene. The asymmetry comes from the potential difference between the layers induced by the substrate. On the other hand, measurements conducted on single-layer graphene did not show any valley current, implying the symmetry persistent in the system.

6.1 Introduction

It is known from many years that similar to charge and spin degree of freedom, the electron has another degree of freedom which is valley. A local minimum in the conduction band or the local maximum in the valance band is referred to as a Valley. This degree of freedom allows the electron to occupy one of the valleys. The study of valley electrons is called Valleytronics [1–4]. An ideal valleytronic material should have two or more degenerate and in-equivalent valleys in its band structure. 2D materials which lack centro-symmetry has two types of valleys in their band diagram which are opposite to each other (K and K′). Thus we can label the electrons in K valley as valley pseudo-spin up and electrons in K′ as valley pseudo-spin down. In such materials, charge carriers from opposite valleys experience an effective magnetic field (Berry curvature)

which is equal in magnitude but opposite in direction (Fig. 6.1a). Berry curvature is derived from the additional phase attained by Bloch electrons, known as Berry's phase. This leads to a phenomenon called valley Hall effect where the electrons residing in the two valleys move to opposite edges of the sample in the presence of an in-plane electric field (Fig. 6.1b).

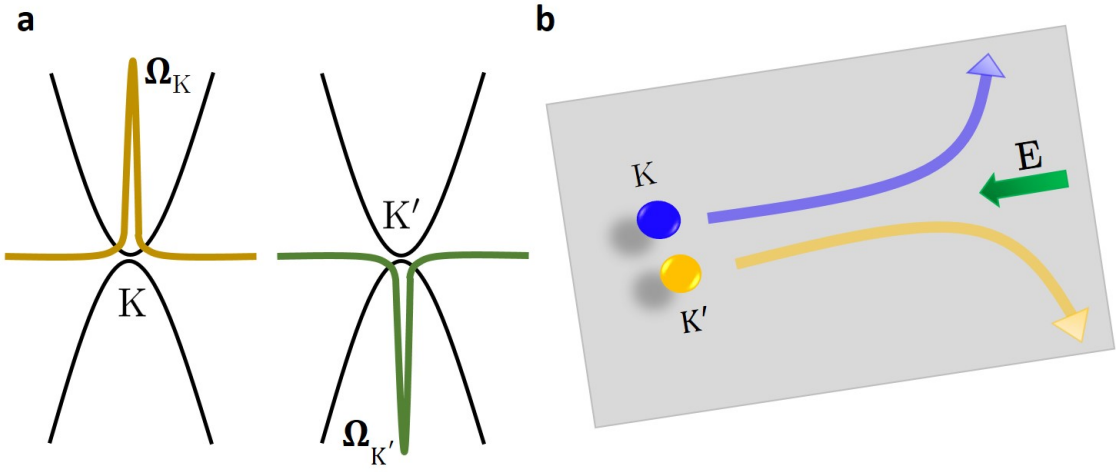

FIGURE 6.1: **a** Schematic representation of the Berry curvature with opposite values at K and K′ high symmetry points of the Brillouin zone. A non-zero Berry curvature is observed only in systems with broken time-reversal symmetry or spatial inversion symmetry. **b** Schematic diagram showing valley Hall effect. In the presence of an in-plane electric field, electrons residing in the two valleys move to opposite edges of the sample due to the opposite polarity of the Berry curvature at the two valleys. Berry curvature, which can be considered as a pseudo magnetic field in the reciprocal space drives the carriers to opposite edges. (This image is partly the same as Fig. 4.1. The image is included here for the reader's convenience).

Valley Hall effect is widely studied in two-dimensional materials including bilayer graphene [42, 43]. However, these studies used a complicated device structure consisting of bilayer graphene sandwiched between hBN layers. In addition, as they could not observe any VHE in ungated bilayer graphene, an electric field had to be applied between the top and bottom gates to break the symmetry between the layers and induce VHE. However, in the current study, we observed VHE in ungated bilayer graphene exfoliated on Si/SiO_2 substrate.

The bilayer and single layer graphene devices are fabricated as follows. The graphene is exfoliated on Si/SiO_2 substrate using the scotch tape method. The number of layers is identified using Raman spectroscopy. Once the number of layers is identified, electron beam lithography followed by electron beam evaporation is used to make contacts. MMA/PMMA resist (positive resist) is used for electron beam lithography. For contacts, 10 nm chromium (Cr) and 60 nm gold (Au) is deposited.

6.2 Local and Non-Local Measurement Method

In order to detect the valley Hall effect in bilayer graphene, the non-local resistance measurement method is used. We have also performed local resistance measurement in order to make a comparison. Fig. 6.2a and b show the schematic representation of the local and non-local resistance measurement respectively. In the local resistance measurement, the current is sent across the length of the device (I_{13}) and the voltage is detected at the two ends of the device (V_{24}). Thus the local resistance is given by,

$$R_L = \frac{V_{24}}{I_{13}} \tag{6.1}$$

On the other hand, in the case of the non-local resistance measurement method, the current is sent across the terminals at one end of the device (I_{12}) and the voltage across the two terminals at the other end is measured (V_{34}). Hence the non-local resistance is given by,

$$R_{NL} = \frac{V_{34}}{I_{12}} \tag{6.2}$$

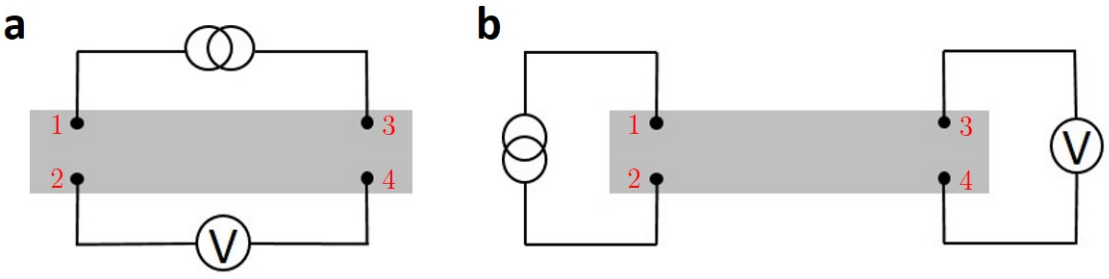

FIGURE 6.2: Schematic illustration of the **a** local and **b** non-local resistance measurement method. In the local resistance measurement, the current is sent across the length of the device and the voltage is detected at the two ends of the device. Whereas in the case of the non-local resistance measurement method, the current is sent across the terminals at one end of the device and the voltage across the two terminals at the other end is measured. (This image is the same as Fig. 3.6. The image is included here for the reader's convenience).

6.3 Valley Hall Effect in Bilayer Graphene

In this study we have investigated the valley Hall effect in bilayer graphene exfoliated on Si/SiO_2 substrate. Fig. 6.3a shows the optical micrograph of the bilayer graphene device (false color is used to enhance the clarity). The local and non-local

resistance measurements are performed using the contacts which are at the two ends of the device (shown schematically in Fig. 6.3b). Fig. 6.3c shows the measured local and non-local resistances for the bilayer graphene device. Following observations can be made from the measurement. One, the intensity of the non-local resistance is much lower than that of the local resistance. This is due to the large distance (12 μm) between the current and voltage terminals in the case of non-local measurement. Second, the non-local resistance is zero at higher positive and negative gate voltages, unlike the local resistance which has a finite value even at higher voltages. This can be explained as follows. At higher negative (positive) voltage, the Fermi level is deep in the valence (conduction) band. The Berry curvature is maximum when the Fermi level is in the gap between the valence and conduction band. The magnitude of the Berry curvature decreases when the Fermi level is moved away from the gap deep to either band. Thus at higher voltages, the carriers experience little or no force as the magnitude of Berry curvature is very small. These observations also affirm the fact that the non-local resistance id indeed due to the valley Hall effect induced by Berry curvature.

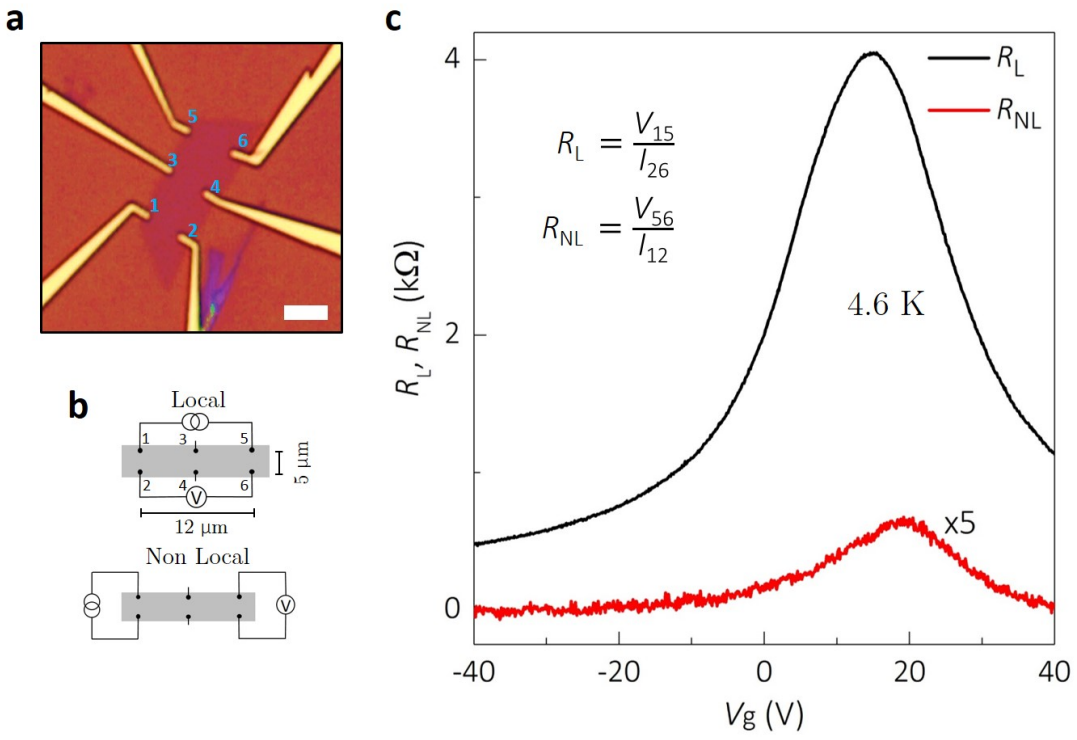

FIGURE 6.3: **a**Optical micrograph of the bilayer graphene device (false colour is used to enhance the clarity). The scale bar is 5 μm. **b** Schematic illustration of the contact configuration used for local and non-local resistance measurements on the device. **c** Measured local and non-local resistances for the bilayer graphene device. The measurement is performed at 4.6 K.

The observation of the valley Hall effect in ungated bilayer graphene is attributed to the emergence of Berry curvature (which is the driving force that pushes the

electrons to the other end of the device) as a result of the layer asymmetry in bilayer graphene. The layer asymmetry comes from the proximity effect where the Si/SiO_2 substrate induces different potentials between the two layers of the bilayer graphene which in turn breaks the layer symmetry in the system.

6.4 Ohmic Contribution to the Local Resistance

Although we have ascertained that the non-local resistance is due to the valley Hall effect, there could be some Ohmic contribution to the non-local resistance which arises from the diffusion of the carriers injected at one end to the other end. This Ohmic contribution to the non-local resistance is given by,

$$R_{Ohmic} = \rho_{xx} e^{-\frac{\pi L}{w}} \tag{6.3}$$

where $\rho_{xx} = R_L(w/L)$. Thus we have calculated the Ohmic contribution and compared it with the non-local resistance (Fig. 6.4). The Ohmic contribution is at least two orders of magnitude smaller than that of the non-local resistance. Hence we rule out the

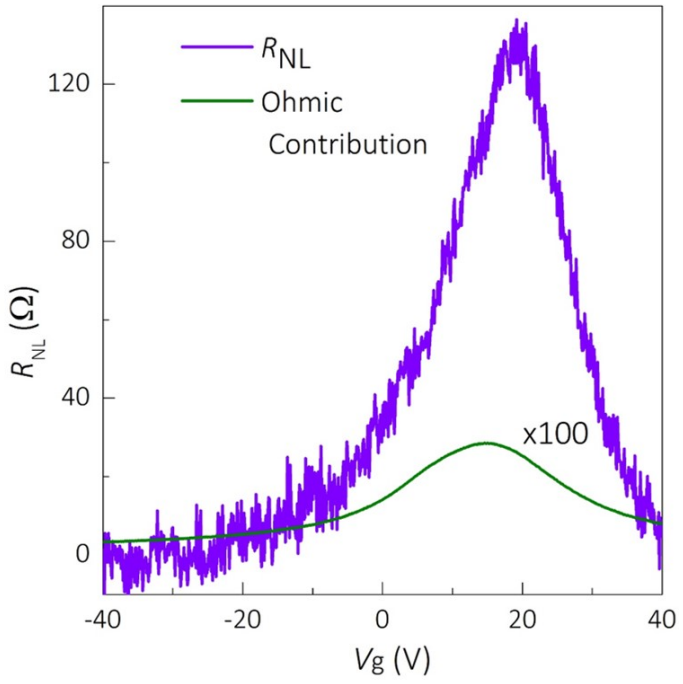

FIGURE 6.4: Ohmic contribution to the non-local resistance calculated using the van der Pauw formula is compared with the measured non-local resistance. The ohmic contribution is at least two orders of magnitude smaller than that of the non-local resistance.

possibility of the diffusion of carriers to the voltage detecting terminals from the current injecting terminals.

6.5 Temperature Dependence of the Local and Non-Local Resistance

We have aslo studied the temperature dependence of the local (Fig. 6.5a) and non-local (Fig. 6.5b) resistance. Both the local and non-local resistance shows thermal activation behaviour. In order to extract more information from these measurements we

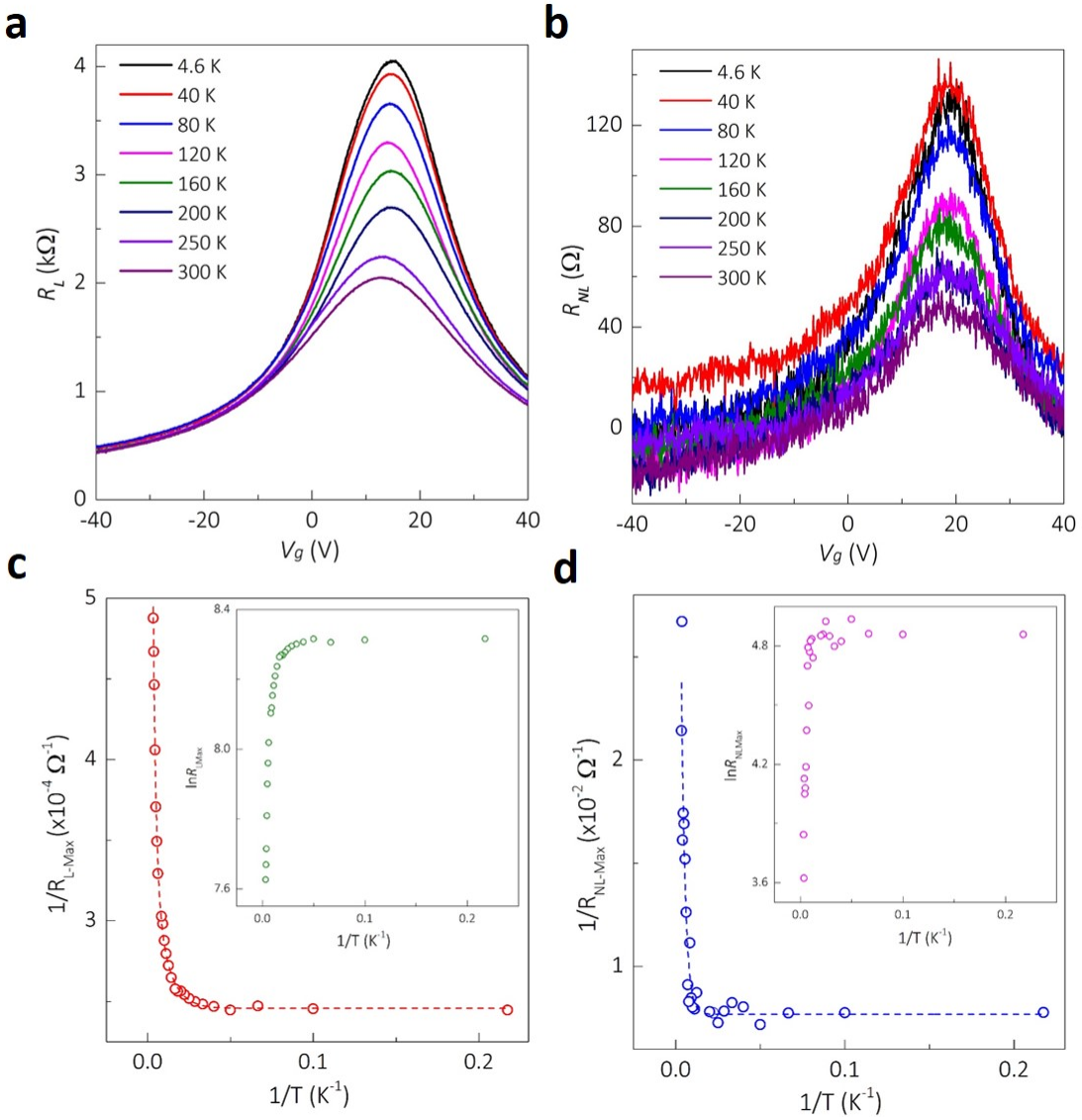

FIGURE 6.5: Temperature dependence measurements for **a** local and **b** non-local resistances. $1/R_{Max}$ versus 1/T plot for **c** local and **d** non-local resistances. The inset of **c** and **d** shows the semi-log plot of resistance with 1/T for local and non-local resistances respectively

have plotted the $1/R_{Max}$ as a function of 1/T for both local (Fig. 6.5c) and non-local (Fig. 6.5d) resistances. The temperature dependence of both the local and non-local resistances were following a double exponential function over the whole temperature range:

$$\frac{1}{R} = \frac{1}{R_1} e^{-\frac{E_1}{k_B T}} + \frac{1}{R_2} e^{-\frac{E_2}{k_B T}} \tag{6.4}$$

where E_1 and E_2 are the activation energy at high temperature and low temperature respectively. The band gap of the sample is twice that of the activation energy at high temperature. We estimated the band gap from the activation energy and is found to be 20 meV. The inset in Fig. 6.5c and Fig. 6.5d shows the semi-log plot of resistance with 1/T. In both the cases it can be seen that at high temperature, band conduction dominates whereas at lower temperatures the conduction is mainly due to hopping.

6.6 Non-Local Measurement in Single Layer Graphene

We have also studied single-layer graphene for valley Hall effect. Fig. 6.6a shows the optical micrograph of the single layer graphene device. The terminal configuration shown in Fig. 6.6b is used to perform the local and non-local resistance

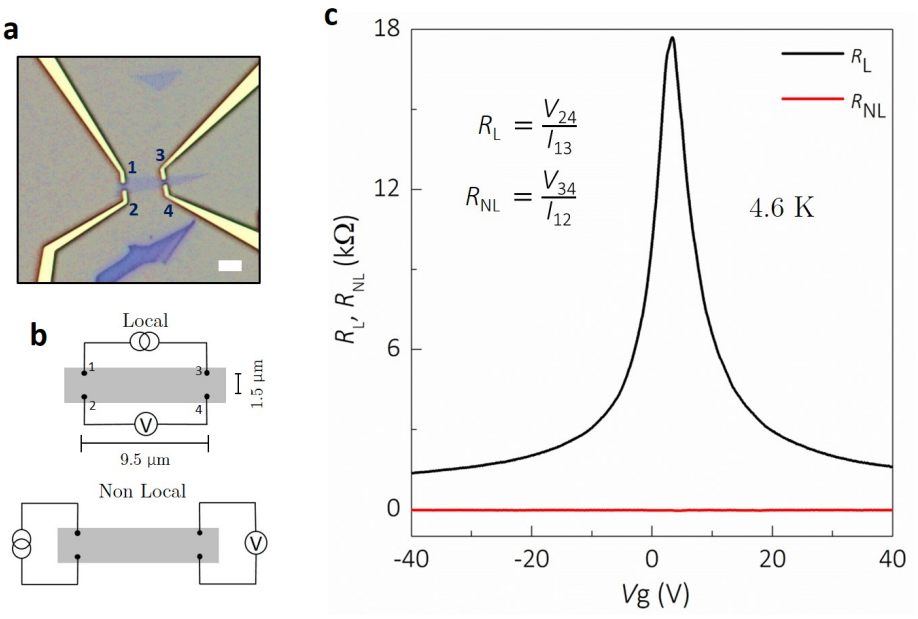

FIGURE 6.6: **a**Optical micrograph of the single layer graphene device (false colour is used to enhance the clarity). The scale bar is 5 μm. **b** Schematic illustration of the contact configuration used for local and non-local resistance measurements on the device. **c** Measured local and non-local resistances for the single layer graphene device. The measurement is performed at 4.6 K.

measurements. Fig. 6.6c shows the measured local and non-local resistance for the single layer graphene at 4.6 K. As can be seen from the figure, single layer graphene exhibit no non-local characteristics although it gives an intense local resistance with charge neutrality point around 5 V. The non observation of nonlocal resistance indicates the presence of symmetry in the system. This also implies that single-layer graphene exfoliated on Si/SiO_2 substrate has zero Berry curvature.

6.7 Summary

We have observed valley Hall effect in ungated bilayer graphene exfoliated on Si/SiO_2 substrate. This is attributed to the emergence of Berry curvature in the system as a result of layer symmetry breaking. The layer asymmetry comes from the proximity effect where the Si/SiO_2 substrate induces different potentials between the two layers of the bilayer graphene. The Ohmic contribution to the non-local resistance was found to be negligible. Both local and non-local resistances shows thermal activation behavior. From temperature dependence resistance measurement it is found that a band gap is opened in the bilayer graphene and is calculated to be 20 meV. The non-local resistance measurement in single layer graphene did not show any sign of valley Hall effect. This indicates that single-layer graphene exfoliated on Si/SiO_2 substrate preserves the symmetry of the system and has zero Berry curvature.

Chapter 7

Conclusion and Future Prospects

In the first part of the work we have theoretically validated the presence of asymmetry in ungated, undoped AB-stacked bilayer graphene with the observation of a non-zero Berry curvature. The asymmetry comes from the spontaneous charge transfer to one of the layers due to long range Coloumb interaction. The polarity of the Berry curvature changes with the sign of layer polarization which can be controlled with the application of an out-of-plane electric field. At higher out-of-plane electric fields of the order of few V/nm, the magnitude of the Berry curvature decreases with the increase in the electric field. This is due to the increase in band gap in bilayer graphene at high electric fields. However, no Berry curvature was observed in AA-stacked bilayer graphene. This indicates the presence of layer symmetry present in the system. Even the application of an out-of-plane electric field could not break the symmetry and induce Berry curvature in AA-stacked bilayer graphene.

We further conducted theoretical studies on the emergence of Berry curvature in hBN-bilayer graphene and hBN-single layer graphene heterostructures for various configurations of the hBN layer. The effect of positive as well as negative out-of-plane electric fields on the magnitude as well as the polarity of the Berry curvature is also studied. In the case of bilayer graphene heterostructure, hBN induces layer asymmetry and hence the Berry curvature. The electric field could manipulate the polarity as well as the magnitude of the Berry curvature depending on the direction of the applied field. On the other hand, the polarity of the Berry curvature could not be reversed with the application of an out-of-plane electric field in hBN single-layer graphene systems although the magnitude of the Berry curvature was dependent on the applied electric field.

Moreover, we have experimentally observed valley Hall effect in ungated bilayer graphene exfoliated on Si/SiO_2 substrate. This is attributed to the emergence

of Berry curvature in the system as a result of layer symmetry breaking. The layer asymmetry comes from the proximity effect where the Si/SiO_2 substrate induces different potentials between the two layers of the bilayer graphene. The Ohmic contribution to the non-local resistance was found to be negligible. From temperature dependence of the measurement it is found that a band gap is opened in the bilayer graphene and is calculated to be 20 meV. However, single layer graphene did not show any sign of valley Hall effect. This indicates that single-layer graphene exfoliated on Si/SiO_2 substrate preserves the symmetry of the system and has zero Berry curvature.

The distinct behavior of electrons in the two equivalent valleys intrinsically as well as towards external perturbation makes them promising to be used to store binary information. But, immense research has to be performed to understand the various aspects of the valley quantum number. Also finding the suitable material for practical applications is a challenging task. Two dimensional materials like graphene, h-BN and Transition Metal Dichalcogenides (TMDs) are suitable candidates for valleytronics study due to the presence of degenerate but inequivalent valleys K and K'. Various valley related properties such as valley Hall effect, valley excitons and valley Zeeman effect are of great scientific importance and worth studying.

Acknowledgements

I would like to express my special appreciation and thanks to my Prof. Hiroshi Mizuta for accepting me as a Ph.D. student in his laboratory. He has been a tremendous mentor for me. The support and freedom he gave me were enormous. I also extend my sincere gratitude to Dr. Manoharan Muruganathan (Senior Lecturer, Mizuta lab). He listened to all my silly queries patiently and curiously and gave me valuable advice. The scientific discussions with him gave me great enthusiasm. He grew the passion for research in me. I would like to thank him for teaching me various *ab initio* packages.

I would like to thank my second supervisor Prof. Yukiko Takamura for her help and support. I am also grateful to my minor supervisor Prof. Yuzuru Takamura for allowing me to do the minor research in his lab. I would like to extend my sincere thanks to Prof. Mikio Koyano for training me on the Raman instrument and for the permission to use the Raman instrument. I would like to acknowledge all the Ph.D. examination committee members, Prof. Mikio Koyano, Prof. Yukiko Takamura, Prof. Masashi Akabori and Prof. Shu Nakaharai (NIMS) for their valuable comments and suggestions.

I am also greatly thankful to the following people for their help and support during Ph.D. my journey. Mr. Innoue Koki taught me SIESTA package. Mr. Marek E. Scmidt taught me python and helped me to familiarize with the Linux operating system. Dr. Koluthungan Jothiramalingam helped me with the basics of measurement. Mr. Gabriel taught me device fabrication. I extend my sincere thanks to Mr. Zhongwang Wang for helping me whenever I had trouble in the clean room. I also had productive discussions with him. I appreciate useful discussions with Dr. Takuya Iwasaki. I am also thankful to my former and present lab mates, Ms. Mayeesha Masrura, Dr. Ahmed Hammam, Dr. Wenzhen Wang, Dr. Huynh Van, Dr. Jaewook Lee, Dr. Fayong Liu, Mr. Guenter Ellrott, Mr. Mohit, Mr. Zheng Zhang, Mr. Hiroya Miyashita, Mr. Seiya Kubo, Mr. Kohei Kobayashi, Mr. Kohei Taketomi, Mr. Syu Nakamura, Mr. Soya Nakano, Mr. Daichi Yoda, Mr. Atsushi Furukawa, Mr. Kazunari Sasaki, Mr. Sho Taniuchi, Mr. Humihiro Seto, Mr. Daiki Kato and Mr. Teruhisa Kanzaki.

I really appreciate the help of Ms. Reiko Seki (Research assistant, Mizuta lab) for her continuous help throughout my Ph.D., especially for official matters.

I am highly indebted to Dr. Shunei Suzuki who was my tutor. He helped me throughout my initial days in Japan getting familiarize with the atmosphere. He was so kind as to help me with Japanese documents whenever necessary. He also made Japanese food for me.

I thank extensively my wife for her incredible support throughout these years. It would have been impossible to complete the Ph.D. without her extraordinary support.

I am highly grateful to my friend Divya for suggesting me the lab for Ph.D. and for her support. I am also overwhelmed with the support of my friends Abhishek and Atif.

Last but not the least, I thank my parents and my family for their love and support.

Bibliography

[1] M. V. Berry. Quantal phase factors accompanying adiabatic changes. *Proc. R. Soc. Lond. A* **392**, 45-57 (1984).

[2] John R. Schaibley, Hongyi Yu, Genevieve Clark, Pasqual Rivera, Jason S. Ross, Kyle L. Seyler, Wang Yao and Xiaodong Xu. Valleytronics in 2D materials. *Nature Reviews Materials* **1**, 16055 (2016).

[3] Xiaodong Xu, Wang Yao, Di Xiao and Tony F. Heinz. Spin and pseudospins in layered transition metal dichalcogenides. *Nature Physics* **10**, 343-350 (2014).

[4] Di Xiao, Wang Yao and Qian Niu. Valley-Contrasting Physics in Graphene: Magnetic Moment and Topological Transport. *Phys. Rev. Lett.* **99**, 236809 (2007).

[5] Di Xiao, Gui-Bin Liu, Wanxiang Feng, Xiaodong Xu and Wang Yao. Coupled Spin and Valley Physics in Monolayers of MoS_2 and Other Group-VI Dichalcogenides. *Phys. Rev. Lett.* **108**, 196802 (2012).

[6] Di Xiao, Ming-Che Chang and Qian Niu. Berry phase effects on electronic properties. *Rev. Mod. Phys.* **82**, 1959 (2010).

[7] K. F. Mak, K. L. McGill, J. Park and P. L. McEuen. The valley Hall effect in MoS_2 transistors. *Science* **344**, 1489-1492 (2014).

[8] Jieun Lee, Kin Fai Mak and Jie Shan. Electrical control of the valley Hall effect in bilayer MoS_2 transistors. *Nature Nanotechnology* **11**, 421-425 (2016).

[9] G. Aivazian, Zhirui Gong, Aaron M. Jones, Rui-Lin Chu, J. Yan, D. G. Mandrus, Chuanwei Zhang, David Cobden, Wang Yao and X. Xu. Magnetic control of valley pseudospin in monolayer WSe_2. *Nature Physics* **11**, 148-152 (2015).

[10] David MacNeill, Colin Heikes, Kin Fai Mak, Zachary Anderson, Andor Korm ányos, Viktor Zólyomi, Jiwoong Park and Daniel C. Ralph. Breaking of Valley Degeneracy by Magnetic Field in Monolayer $MoSe_2$. *Phys. Rev. Lett.* **114**, 037401 (2015).

[11] S. Pancharatnam. Generalized theory of interference, and its applications. *Proceedings of the Indian Academy of Sciences - Section A* **44**, 247-262 (1956).

[12] Stephen T. Thornton and Jerry B. Marion. Classical Dynamics of Particles and Systems. Cengage Learning, 2014.

[13] David J. Griffiths. Introduction to Quantum Mechanics. Prentice Hall, 1994

[14] K. S. Novoselov, A. K. Geim, S. V. Morozov, D. Jiang, Y. Zhang, S. V. Dubonos, I. V. Grigorieva and A. A. Firsov. Electric Field Effect in Atomically Thin Carbon Films. *Science* **306**, 666-669 (2004).

[15] K. S. Novoselov, D. Jiang, F. Schedin, T. J. Booth, V. V. Khotkevich, S. V. Morozov, and A. K. Geim. Two-dimensional atomic crystals. *Proc. Nat l. Acad. Sci. U.S.A* **102**, 10451–10453 (2005).

[16] K. S. Novoselov, A. K. Geim, S. V. Morozov, D. Jiang, M. I. Katsnelson, I. V. Grigorieva, S. V. Dubonos and A. A. Firsov. Two-dimensional gas of massless Dirac fermions in graphene. *Nature* **438**, 197–200 (2005).

[17] A. K. Geim and K. S. Novoselov. The rise of graphene. *Nature Materials* **6**, 183-191 (2007).

[18] F. Schedin, A. K. Geim, S. V. Morozov, E. W. Hill, P. Blake, M. I. Katsnelson and K. S. Novoselov. Detection of individual gas molecules adsorbed on graphene. textitNature Materials **6**, 652–655 (2007).

[19] Yu-Ming Lin, Keith A. Jenkins, Alberto Valdes-Garcia, Joshua P. Small, Damon B. Farmer and Phaedon Avouris. Operation of Graphene Transistors at Gigahertz Frequencies. *Nano Lett.* **9**(1), 422–426 (2009).

[20] Yuanbo Zhang, Yan-Wen Tan, Horst L. Stormer and Philip Kim. Experimental observation of the quantum Hall effect and Berry's phase in graphene. *Nature* **438**, 201-204 (2005).

[21] Xinjie Wang, Jonathan R. Yates, Ivo Souza and David Vanderbilt, *Ab initio* calculation of the anomalous Hall conductivity by Wannier interpolation. Phys. Rev. B **74**, 195118 (2006).

[22] Please see Ref. [21] for detailed derivation.

[23] Yugui Yao, Leonard Kleinman, A. H. MacDonald, Jairo Sinova, T. Jungwirth, Dingsheng Wang, Enge Wang, and Qian Niu, First Principles Calculation of Anomalous Hall Conductivity in Ferromagnetic bcc Fe. Phys. Rev. Lett. **92**, 037204 (2004).

[24] Vitale, Steven A. and Nezich, Daniel and Varghese, Joseph O. and Kim, Philip and Gedik, Nuh and Jarillo-Herrero, Pablo and Xiao, Di and Rothschild, Mordechai, Valleytronics: Opportunities, Challenges, and Paths Forward. Small **14**, 1801483 (2018).

[25] K. S. Novoselov, A. Mishchenko, A. Carvalho and A. H. Castro Neto, 2D materials and van der Waals heterostructures. Science **353**, 6298 (2016).

[26] K. F. Mak, K. L. McGill, J. Park and P. L. McEuen, The valley Hall effect in MoS_2 transistors. Science **344**, 1489 (2014).

[27] Jieun Lee, Kin Fai Mak and Jie Shan, Electrical control of the valley Hall effect in bilayer MoS_2 transistors. Nat. Nanotechnol. **11**, 421 (2016).

[28] O. Gunawan, Y. P. Shkolnikov, K. Vakili, T. Gokmen, E. P. De Poortere and M. Shayegan, Valley Susceptibility of an Interacting Two-Dimensional Electron System. Phys. Rev. Lett. **97**, 186404 (2006).

[29] Wang Yao, Di Xiao and Qian Niu, Valley-dependent optoelectronics from inversion symmetry breaking. Phys. Rev. B **77**, 235406 (2008).

[30] Edward McCann, Asymmetry gap in the electronic band structure of bilayer graphene. Phys. Rev. B **74**, 161403(R) (2006).

[31] Eduardo V. Castro, K. S. Novoselov, S. V. Morozov, N. M. R. Peres, J. M. B. Lopes dos Santos, Johan Nilsson, F. Guinea, A. K. Geim and A. H. Castro Neto, Biased Bilayer Graphene: Semiconductor with a Gap Tunable by the Electric Field Effect. Phys. Rev. Lett. **99**, 216802 (2007).

[32] Hongki Min, Bhagawan Sahu, Sanjay K. Banerjee and A. H. MacDonald, *Ab initio* theory of gate induced gaps in graphene bilayers. Phys. Rev. B **75**, 155115 (2007).

[33] Yuanbo Zhang, Tsung-Ta Tang, Caglar Girit, Zhao Hao, Michael C. Martin, Alex Zettl, Michael F. Crommie, Y. Ron Shen and Feng Wang, Direct observation of a widely tunable bandgap in bilayer graphene. Nature **459**, 820 (2009).

[34] Hongki Min, Giovanni Borghi, Marco Polini and A. H. MacDonald, Pseudospin magnetism in graphene. Phys. Rev. B **77**, 041407(R) (2008).

[35] Fan Zhang, Hongki Min, Marco Polini and A. H. MacDonald, Spontaneous inversion symmetry breaking in graphene bilayers. Phys. Rev. B **81**, 041402(R) (2010).

[36] Jeil Jung, Fan Zhang and Allan H. MacDonald, Lattice theory of pseudospin ferromagnetism in bilayer graphene: Competing interaction-induced quantum Hall states. Phys. Rev. B **83**, 115408 (2011).

[37] Yuanbo Zhang and Tsung-Ta Tang and Caglar Girit and Zhao Hao and Michael C. Martin and Alex Zettl and Michael F. Crommie and Y. Ron Shen and Feng Wang, Direct observation of a widely tunable bandgap in bilayer graphene. Nature **459**, 820-823 (2009).

[38] Weitz, R. T. and Allen, M. T. and Feldman, B. E. and Martin, J. and Yacoby, A., Broken-Symmetry States in Doubly Gated Suspended Bilayer Graphene. Science **330**, 812-816 (2010).

[39] Velasco Jr, J. and Jing, L. and Bao, W. and Lee, Y. and Kratz, P. and Aji, V. and Bockrath, M. and Lau, C. N. and Varma, C. and Stillwell, R. and Smirnov, D. and Zhang, Fan and Jung, J. and MacDonald, A. H., Transport spectroscopy of symmetry-broken insulating states in bilayer graphene. Nature Nanotechnology **7**, 156-160 (2012).

[40] Bao, Wenzhong and Velasco, Jairo and Zhang, Fan and Jing, Lei and Standley, Brian and Smirnov, Dmitry and Bockrath, Marc and MacDonald, Allan H. and Lau, Chun Ning, Evidence for a spontaneous gapped state in ultraclean bilayer graphene. PNAS **109**, 10802-10805 (2012).

[41] BZhang, Fan and Jung, Jeil and Fiete, Gregory A. and Niu, Qian and MacDonald, Allan H., Spontaneous quantum Hall states in chirally stacked few-layer graphene systems. Phys. Rev. Lett. **106**, 156801 (2011).

[42] Mengqiao Sui, Guorui Chen, Liguo Ma, Wen-Yu Shan, Dai Tian, Kenji Watanabe, Takashi Taniguchi, Xiaofeng Jin, Wang Yao, Di Xiao and Yuanbo Zhang, Gate-tunable topological valley transport in bilayer graphene. Nat. Phys. **11**, 1027 (2015).

[43] Y. Shimazaki, M. Yamamoto, I. V. Borzenets, K. Watanabe, T. Taniguchi and S. Tarucha, Generation and detection of pure valley current by electrically induced Berry curvature in bilayer graphene. Nat. Phys. **11**, 1032 (2015).

[44] P. Recher, B. Trauzettel, A. Rycerz, Ya. M. Blanter, C. W. J. Beenakker and A. F. Morpurgo, Aharonov-Bohm effect and broken valley degeneracy in graphene rings. Phys. Rev. B **76**, 235404 (2007).

[45] A. Rycerz, J. Tworzydło and C. W. J. Beenakker, Valley filter and valley valve in graphene. Nat. Phys. **3**, 172 (2007).

[46] Ivar Martin, Ya. M. Blanter and A. F. Morpurgo, Topological Confinement in Bilayer Graphene. Phys. Rev. Lett. **100**, 036804 (2008).

[47] Jiang,Xueping and Kharche,Neerav and Kohl,Paul and Boykin,Timothy B. and Klimeck,Gerhard and Luisier,Mathieu and Ajayan,Pulickel M. and Nayak,Saroj K., Giant quasiparticle bandgap modulation in graphene nanoribbons supported on weakly interacting surfaces. Appl. Phys. Lett. **103**, 133107 (2013).

[48] José M Soler, Emilio Artacho, Julian D Gale, Alberto García, Javier Junquera, Pablo Ordejón and Daniel Sánchez-Portal, The SIESTA method for *ab initio* order-N materials simulation. J. Phys.: Condens. Matter **14**, 2745 (2002).

[49] M. Dion, H. Rydberg, E. Schröder, D. C. Langreth and B. I. Lundqvist, Van der Waals Density Functional for General Geometries. Phys. Rev. Lett. **14**, 246401 (2004).

[50] Ivo Souza, Nicola Marzari and David Vanderbilt, Maximally localized Wannier functions for entangled energy bands. Phys. Rev. B **65**, 035109 (2001).

[51] Paolo Giannozzi, Stefano Baroni, Nicola Bonini, Matteo Calandra, Roberto Car, Carlo Cavazzoni, Davide Ceresoli, Guido L Chiarotti, Matteo Cococcioni, Ismaila Dabo, Andrea Dal Corso, Stefano de Gironcoli, Stefano Fabris, Guido Fratesi, Ralph Gebauer, Uwe Gerstmann, Christos Gougoussis, Anton Kokalj, Michele Lazzeri, Layla Martin-Samos, Nicola Marzari, Francesco Mauri, Riccardo Mazzarello, Stefano Paolini, Alfredo Pasquarello, Lorenzo Paulatto, Carlo Sbraccia, Sandro Scandolo, Gabriele Sclauzero, Ari P Seitsonen, Alexander Smogunov, Paolo Umari and Renata M Wentzcovitch, QUANTUM ESPRESSO: a modular and open-source software project for quantum simulations of materials. J. Phys.: Condens. Matter **21**, 395502 (2009).

[52] John P. Perdew, Kieron Burke and Matthias Ernzerhof, Generalized Gradient Approximation Made Simple. Phys. Rev. Lett. **77**, 3865 (1996).

[53] Stefan Grimme, Semiempirical GGA-type density functional constructed with a long-range dispersion correction. J. Comp. Chem. **27**, 1787 (2006).

[54] Yuanbo Zhang, Yan-Wen Tan, Horst L. Stormer and Philip Kim, Experimental observation of the quantum Hall effect and Berry's phase in graphene. Nature **438**, 201-204 (2005).

[55] K. S. Novoselov, E. McCann, S. V. Morozov, V. I. Fal'ko, M. I. Katsnelson, U. Zeitler, D. Jiang, F. Schedin and A. K. Geim, Unconventional quantum Hall effect and Berry's phase of 2π in bilayer graphene. Nat. Phy. **2**, 177-180 (2006).

[56] K. F. Mak, K. L. McGill, J. Park and P. L. McEuen, The valley Hall effect in MoS_2 transistors. Science **344**, 1489 (2014).

[57] R. V. Gorbachev *et al.*, Detecting topological currents in graphene superlattices. Science **346**, 448-451 (2014).

[58] Yugui Yao, Leonard Kleinman, A. H. MacDonald, Jairo Sinova, T. Jungwirth, Ding-sheng Wang, Enge Wang and Qian Niu, Phys. Rev. Lett. **92**, 037204 (2004).

[59] Xinjie Wang, David Vanderbilt, Jonathan R. Yates and Ivo Souza, Phys. Rev. B **76**, 195109 (2007).

[60] K. Afsal *et al.*, Electrically controlled valley states in bilayer graphene

List of Publications

Journal Publications

1. K. Afsal, M. Manoharan and H. Mizuta
   Electrically Controlled Valley States in Bilayer Graphene
   (Submitted)

2. K. Afsal, M. Manoharan and H. Mizuta
   Manipulating Berry curvature in hBN-Bilayer graphene heterostructure
   (In preparation)

3. K. Afsal, M. Manoharan and H. Mizuta
   Substrate induced valley Hall effect in bilayer graphene
   (In preparation)

International Conferences

1. K. Afsal, M. Manoharan and H. Mizuta
   Valley Hall Effect in unbiased Bilayer Graphene
   The 21^{st} International Conference on Electron Dynamics in Semiconductors, Optoelectronics and Nanostructures, July 14-19, 2019, Nara, Japan (Accepted).

2. K. Afsal, M. Manoharan and H. Mizuta
   Experimental Study of the Valley States in Bilayer Graphene
   International Workshop Spintronics and Valleytronics of Two-dimensional Materials, May 20-24, 2019, PCS IBS, Daejeon, Korea.

Domestic Conferences

1. K. Afsal, M. Manoharan and H. Mizuta
   Evolution of p_z Orbital with out-of-plane Electric Field in Bilayer Graphene
   The 65^{th} JSAP Spring Meeting, March 17-20, 2018, Tokyo, Japan (Oral Presentation).

2. K. Afsal, M. Manoharan and H. Mizuta
   First-Principle Study of Bilayer Graphene Valley States.
   The 79^{th} JSAP Autumn Meeting, September 18-21, 2018, Nagoya, Japan (Oral Presentation)

3. K. Afsal, M. Manoharan and H. Mizuta
   Berry Curvature Study of hBN-Bilayer Graphene Heterostructure.
   The 66^{th} JSAP Spring Meeting, March 09-12, 2019, Tokyo, Japan (Oral Presentation)